Tectonics®

RESEARCH ARTICLE
10.1029/2023TC008032

Key Points:

- New thermochronologic data constrain rapid exhumation of the Pinaleño metamorphic core complex to ca. 27–21 Ma
- The Pinaleño Mountains experienced renewed tectonic exhumation from 13.5 to 11 Ma during Basin and Range-style extension
- Plate margin dynamics and local magmatism exert a primary influence on spatiotemporal patterns of core complex exhumation

Supporting Information:

Supporting Information may be found in the online version of this article.

Correspondence to:

J. B. Chapman,
jbchapmanv@utep.edu

Citation:

Chapman, J. B., Scoggin, S. H., Jepson, G., Ricketts, J. W., Schaen, A. J., & Trzinski, A. E. (2024). Oligocene-Miocene exhumation of the Pinaleño metamorphic core complex, southeastern Arizona: Support for magmatism and plate margin reorganization as controls on regional exhumation trends. *Tectonics*, *43*, e2023TC008032. https://doi.org/10.1029/2023TC008032

Received 26 JULY 2023
Accepted 19 MAR 2024

Author Contributions:

Conceptualization: James B. Chapman
Data curation: James B. Chapman
Formal analysis: James B. Chapman, Shane H. Scoggin, Gilby Jepson, Jason W. Ricketts, Allen J. Schaen
Funding acquisition: James B. Chapman
Investigation: James B. Chapman, Shane H. Scoggin, Jason W. Ricketts, Adam E. Trzinski
Methodology: James B. Chapman, Gilby Jepson, Jason W. Ricketts, Allen J. Schaen
Resources: James B. Chapman
Supervision: James B. Chapman
Validation: Allen J. Schaen
Visualization: Shane H. Scoggin, Gilby Jepson, Jason W. Ricketts, Allen J. Schaen

Oligocene-Miocene Exhumation of the Pinaleño Metamorphic Core Complex, Southeastern Arizona: Support for Magmatism and Plate Margin Reorganization as Controls on Regional Exhumation Trends

James B. Chapman[1], Shane H. Scoggin[2], Gilby Jepson[3], Jason W. Ricketts[1], Allen J. Schaen[4], and Adam E. Trzinski[5]

[1]Department of Earth, Environmental and Resource Sciences, University of Texas at El Paso, El Paso, TX, USA, [2]School of the Environment, Washington State University, Pullman, WA, USA, [3]School of Geosciences, University of Oklahoma, Norman, OK, USA, [4]Department of Geosciences, University of Arizona, Tucson, AZ, USA, [5]Department of Geology and Geophysics, University of Wyoming, Laramie, WY, USA

Abstract The Pinaleño Mountains of southeastern Arizona is the eastern-most metamorphic core complex in the southern U.S. and northern Mexican Cordillera. This study investigates the thermal history and exhumation record of the Pinaleño core complex using mica $^{40}Ar/^{39}Ar$, apatite and zircon (U-Th)/He, and apatite fission-track thermochronometers. The Pinaleño Mountains experienced two periods of rapid cooling during the Cenozoic. The first period, from ca. 27 to 21 Ma, records tectonic exhumation related to the development of the core complex and extensional shear zone. This period was followed by a relatively quiescent interval from 21 to 13.5 Ma that records little to no exhumation. The second period of rapid cooling, from 13.5 to 11 Ma, records tectonic exhumation related to high-angle normal faulting, characteristic of the Basin and Range province. The exhumation timing of the Pinaleño core complex matches previously recognized spatiotemporal trends in the southern Basin and Range province and indicates that core complex exhumation in this region started in southeastern Arizona (ca. 32–33°N) and migrated both northward and southward. These trends correlate well with the latitude and timing of subduction of the Pacific-Farallon spreading ridge and the migration of the Mendocino (northward) and Rivera (southward) triple junctions. Spatiotemporal core complex exhumation trends also correlate well with regional magmatism associated with the mid-Cenozoic flare-up, including syn-extensional intrusive rocks found in the footwalls of core complexes.

1. Introduction

The North American Cordillera is an archetypal example of an orogen that experienced syn- to post-orogenic collapse, accommodated by the development of continental metamorphic core complexes that exhumed mid-crustal rocks to the surface and accommodated large-magnitude extensional strain (Coney, 1980; Coney & Harms, 1984; Foster & John, 1999; Platt et al., 2015; Whitney et al., 2013) (Figure 1). These core complexes are central to many tectonic models, however, the geodynamic mechanisms and forces that generated them remain the subject of debate. End-member hypotheses for core complex formation in North America include (a) orogenic collapse due to excess gravitational potential energy following the termination of orogenesis, (b) changes in plate boundary conditions with regional stress fields transitioning from compressional to extensional, (c) opening of a slab window in the subducting Farallon plate, (d) Farallon slab roll-back and/or foundering, and (e) thermal weakening and viscosity decrease of the crust due to enhanced heat flow from increased asthenospheric upwelling and regional magmatism (Armstrong & Ward, 1991; Atwater, 1970; Bahadori et al., 2022; Coney, 1987; Coney & Harms, 1984; Dickinson & Snyder, 1979; Dokka & Ross, 1995; Gans et al., 1989; Glazner & Bartley, 1984; Gottardi et al., 2020; Howlett et al., 2021; Jepson et al., 2022; Konstantinou, 2022; Lund-Snee & Miller, 2022; Rey et al., 2009; Sonder & Jones, 1999; Zuza & Cao, 2023).

One of the key data sets used to evaluate hypotheses for core complex formation is the timing of extension and tectonic exhumation of core complex footwalls. Recent data compilations show that extension and exhumation are diachronous across the Cordillera and generally become younger from the northern to central core complex belt and becomes younger from south to north in the southern belt (Chapman et al., 2021; Howlett et al., 2021; Konstantinou & Miller, 2015; Zuza & Cao, 2023). The spatiotemporal trend in the southern belt appears to reverse in southeast Arizona, U.S., where core complex exhumation is older than is recorded in Sonora, Mexico

Writing – original draft: James B. Chapman, Shane H. Scoggin
Writing – review & editing: James B. Chapman, Shane H. Scoggin, Gilby Jepson, Jason W. Ricketts, Allen J. Schaen

(Granillo & Calmus, 2003; Haines & van der Pluijm, 2008; Jacobson et al., 2019; Miranda-Gasca et al., 1998; Nourse et al., 1994; Wong & Gans, 2008; Wong et al., 2010) (Figure 2).

In this study, we employ low-temperature thermochronology to address the time-temperature history of the footwall of the Pinaleño Mountains (Dził Nnilchí' Diyiléé; Western Apache), located in southeast Arizona, USA (Figure 3). The Pinaleño Mountains represent the easternmost, farthest inland core complex in the region and are located at the junction where regional exhumation age trends appear to reverse, becoming younger to both the south and north. New zircon and apatite (U-Th)/He (ZHe, AHe), apatite fission track (AFT), and white mica and biotite $^{40}Ar/^{39}Ar$ thermochronologic data constrain the timing of exhumation of the Pinaleño core complex and contribute to the debate surrounding geodynamic driving mechanisms in the North American Cordillera. These data suggest that a combination of processes likely contributed to formation of core complexes in southern Arizona.

2. Geologic Setting of the Pinaleño Metamorphic Core Complex

The Pinaleño Mountains are bounded to the east by the Pinaleño detachment fault, which is buried in the Safford Basin, but exposed in the Santa Teresa Mountains where it is called the Black Rock detachment fault (Figure 3) (Davis & Hardy, 1981; Kruger & Johnson, 1994; Long et al., 1995; Thorman & Naruk, 1987). An ~1 km-thick mylonitic shear zone is exposed along the northeast range front in the footwall of the Pinaleño-Black Rock detachment fault, which records top-to-the northeast movement (Bailey & Eyster, 2003; Long et al., 1995; Naruk, 1986; Thorman & Naruk, 1987). Reflection seismic data form the Safford Basin indicates that the mylonitic shear zone extends from the surface into the mid-crust and is locally cross-cut by a range-bounding, high-angle normal fault (Kruger & Johnson, 1994; Kruger et al., 1995). This high-angle normal fault is not exposed at the surface.

Metamorphic and igneous rocks in the footwall of the Pinaleño core complex include the 1.7 Ga Pinal Schist (Meijer, 2014), 1.6 Ga granodiorites and granites (equivalent to the Johnny Lyon granodiorite e.g., Cooper & Silver, 1964), 1.4 Ga Oracle granite (Long et al., 1995), 1.1 Ga diabase dikes (Bright et al., 2014), the ~55 Ma Relleno suite (Long et al., 1995; Scoggin, Chapman, et al., 2021), and Oligocene intrusions including the Gillespie granite and the Goodwin Canyon quartz monzonite (Long et al., 1995; Nickerson, 2012). The hanging wall of the core complex contains brittlely deformed Paleozoic–Cenozoic sediments, including the ca. 29–27 Ma Galiuro Volcanics, interpreted to have erupted synchronously with regional extension and exhumation of the core complex (Arca et al., 2010; Creasey et al., 1977; Davis & Hardy, 1981).

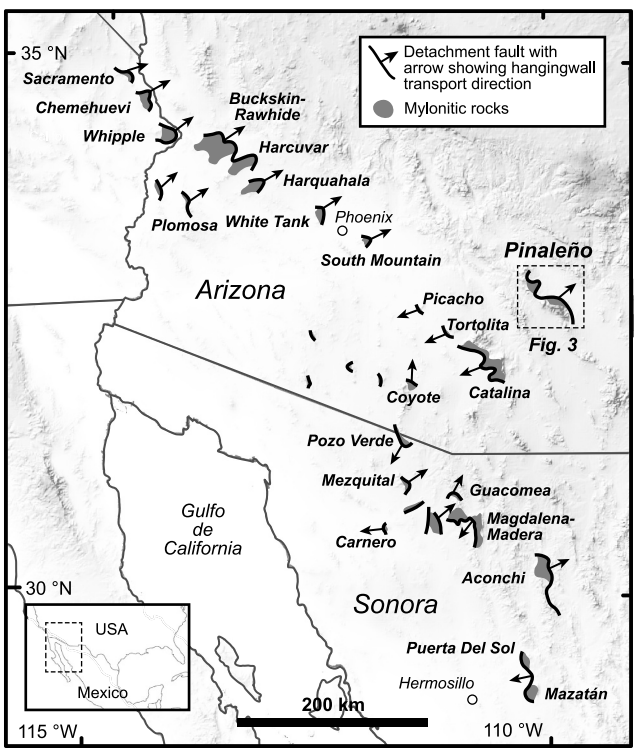

Figure 1. Overview map of the southern belt of metamorphic core complexes in the North American Cordillera. Modified from Chapman et al. (2021).

No comprehensive study of the Pinaleño Mountains exhumation history has been previously undertaken, although thermochronologic data has been reported from the Pinaleño core complex footwall including a whole-rock (mylonite) K-Ar date of 28 Ma (Rehrig & Reynolds, 1980), a muscovite $^{40}Ar/^{39}Ar$ date of 23.5 Ma and a biotite $^{40}Ar/^{39}Ar$ date of 19.8 Ma from an undeformed Relleno suite granite sample (sample PM-3, Long et al., 1995), two biotite $^{40}Ar/^{39}Ar$ ages of 18.5 and 28.6 Ma from mylonite rocks (samples PM-4 and PM-6, Long et al., 1995), three AFT dates of 29.2, 25, and 19.6 Ma that decrease with decreasing elevation (Jepson et al., 2021), and Fe-oxide (U-Th)/He dates in the range 25–9 Ma (Scoggin, Reiners, et al., 2021). These dates are similar to data from other local core complexes, including the Catalina-Rincon and Coyote Mountains core complexes (Fayon et al., 2000; Gottardi et al., 2020; Jepson et al., 2022).

2.1. Sample Descriptions

All samples in this study are igneous rocks from the footwall of the Pinaleño Mountains, collected from a range of elevations (Table 1). Samples SS-20-08, SS-20-09, and SS-20-10 are non-deformed to weakly foliated monzogranites from the ~1.4 Ga Oracle granite. These three samples were taken from higher elevations (>1,800 m) compared to other samples and located structurally

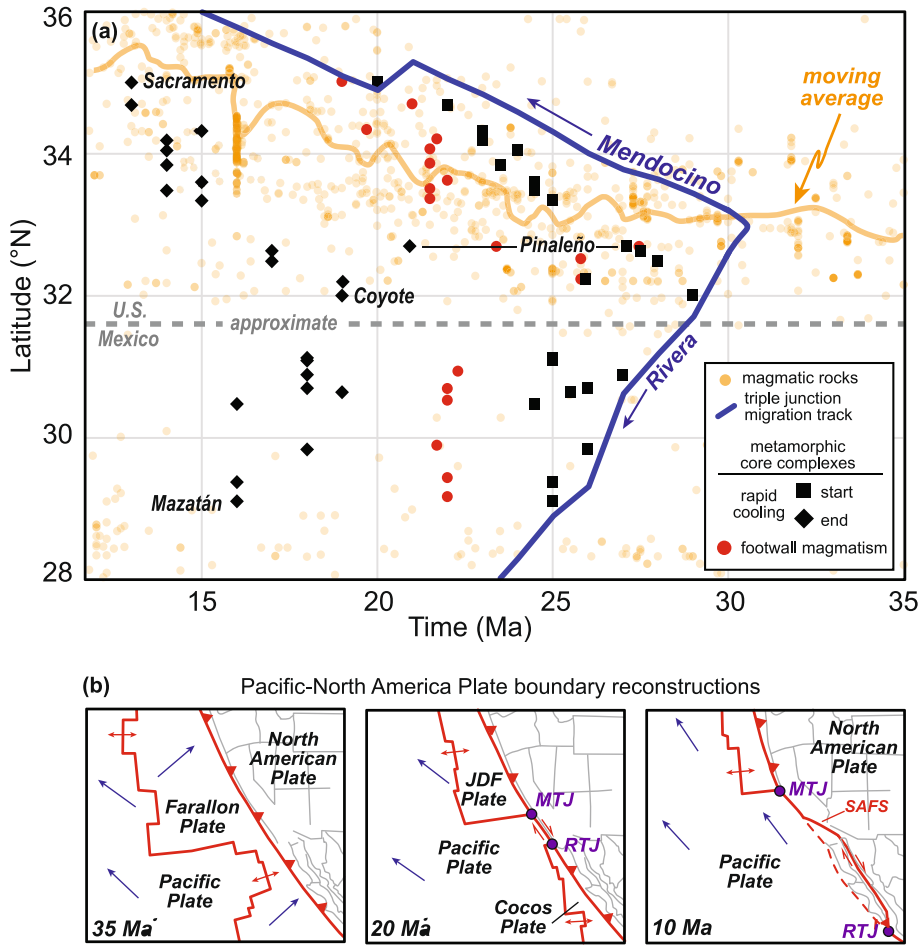

Figure 2. (a) Latitude versus time plot for the southern Basin and Range province with data from longitude 106–117.5°W. Blue lines show the reconstructed position of the Mendocino and Rivera triple junctions (MTJ and RTJ) relative to the North American plate. The orange line is a moving average (period = 50) of magmatic dates compiled from EarthChem. The start and end of rapid cooling for metamorphic core complexes is reported in Foster and Spencer (1992), John and Foster (1993), Fitzgerald et al. (1993), Miranda-Gasca et al. (1998), Pease et al. (1999), Granillo and Calmus (2003), Haines and van der Pluijm (2008), Carter et al. (2004), Wong and Gans (2008), Wong et al. (2010), Singleton et al. (2014, 2019), Prior et al. (2016), LaForge et al. (2017), Jacobson et al. (2019), Gottardi et al. (2020), and Jepson et al. (2022). (b) Schematic plate reconstructions showing the subduction of the Pacific-Farallon spreading ridge, the initiation of the MTJ and RTJ, the development of the dextral-transform Pacific-North American plate boundary, and the San Andreas Fault system (SAFS). Modified from Atwater and Stock (1998). The Juan de Fuca (JDF) plate and Cocos plate are remnants of the Farallon plate. Blue arrows are reconstructed plate motion vectors.

beneath the mylonite zone. Samples ASH-1A, SS-20-04, and SS-20-06 were collected from within the mylonite zone and are located at lower elevations (<1,800 m). Sample SS-20-04 comes from a partially melted diabase enclave entrained in the Relleno suite and has a crystallization age of 1.1 Ga (Scoggin, Chapman, et al., 2021). Sample ASH-1A is a weakly mylonitized monzodiorite and sample SS-20-06 is a weakly mylonitized granodiorite, both part of the ca. 55 Ma Relleno suite (Scoggin, Chapman, et al., 2021).

3. Methods

Apatite, zircon, white mica, and biotite were separated using standard methods involving crushing and grinding, a Wilfley table, magnetic separation, heavy liquid separation, static isolation for micas, and hand-picking under a binocular microscope. Biotite and muscovite samples were washed in DI water in a sonicator to remove excess detritus prior to irradiation.

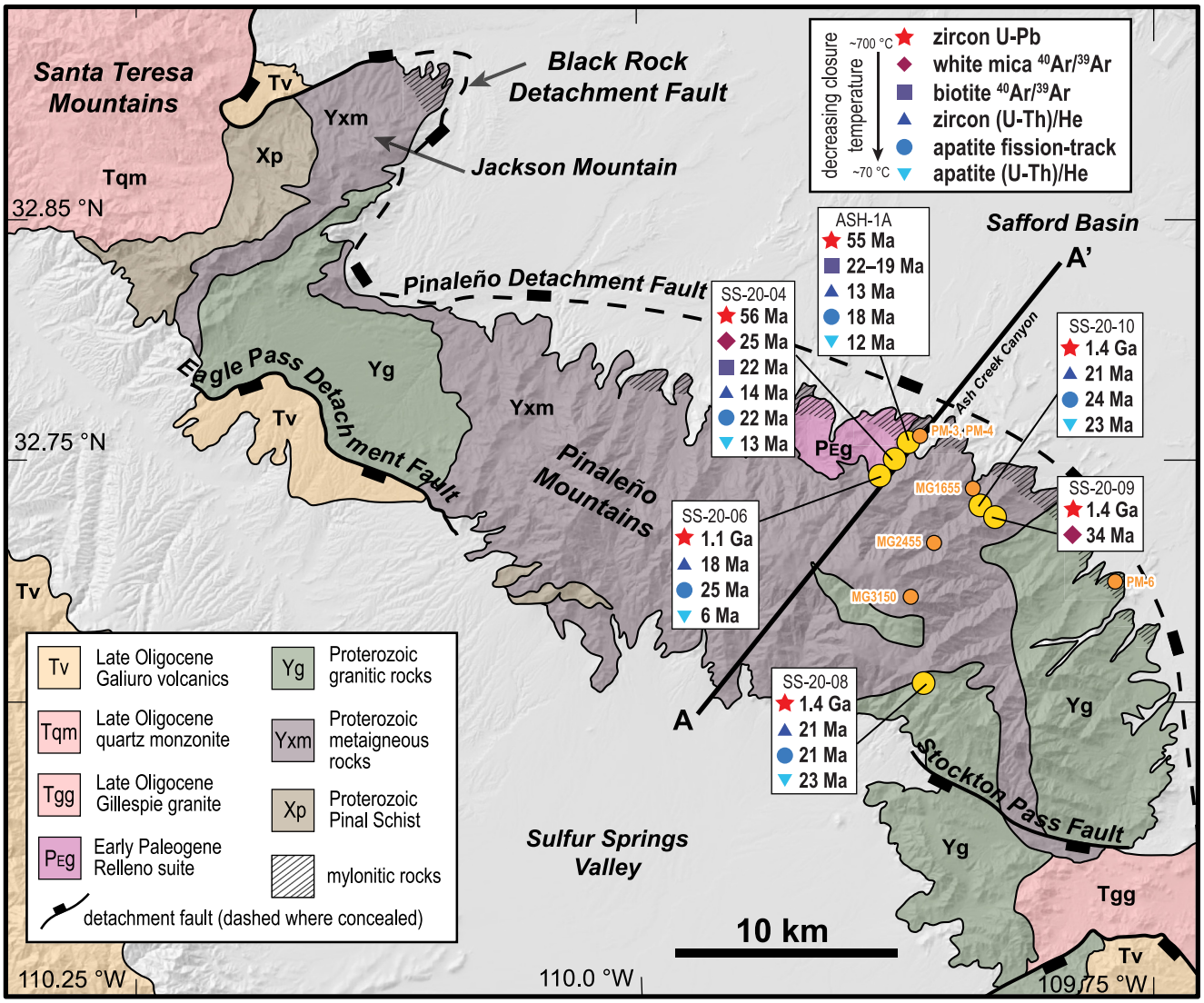

Figure 3. Simplified geologic map of the Pinaleño core complex modified after Thorman and Naruk (1987) and Drewes (1996). Sample locations from this study are shown by large yellow circles with corresponding thermochronological data. Samples from previous studies (Jepson et al., 2021; Long et al., 1995) mentioned in the text are shown by small orange circles. Cross-section A-A' is presented in Figure 7.

3.1. Mica $^{40}Ar/^{39}Ar$ Thermochronology

$^{40}Ar/^{39}Ar$ incremental heating experiments were performed at the University of Arizona Noble Gas Laboratory (Figure 4). Muscovite and biotite samples were sieved to separate grain sizes between 350 and 600 μm and hand-picked to avoid altered grains or inclusions. Purified separates were wrapped in aluminum foil, placed in 2.5 cm aluminum disks, and irradiated along with the 28.201 Ma Fish Canyon sanidine standard (Kuiper et al., 2008) at the Oregon State University TRIGA reactor in the Cadmium-Lined In-Core Irradiation Tube. Approximately 2–4 mg of each separate was placed in a 5 mm well within a copper planchette and incrementally heated with a 55 W CO_2 laser. Extracted gas was cleaned for 20–30 min using two SEAS GP50 getter at 450°C, one SAES NP10 getter at room temperature, and an Edwards Polycold® PCC Compact Cooler maintained at −90°C before being analyzed using an ARGUS VI multicollector noble gas mass spectrometer. $^{40}Ar/^{39}Ar$ dates are calculated using the decay constants of Min et al. (2000) and analytical uncertainties including J contributions, are reported at 2σ. Samples were corrected using an atmospheric $^{40}Ar/^{36}Ar$ value of 298.56 ± 0.31 (Lee et al., 2006). Data reduction was performed using Pychron software (Ross, 2019) and supplemental data reporting follows Schaen et al. (2021).

Table 1
Location, Elevation, Geo- and Thermochronological Data of Rock Samples

Sample	Latitude (°N)	Longitude (°W)	Elevation (m)	Zircon U-Pb (Ma)	White mica $^{40}Ar/^{39}Ar$ (Ma)	Biotite $^{40}Ar/^{39}Ar$ (Ma)	Zircon (U-Th)/He (Ma)	Apatite fission-track (Ma)	Apatite (U-Th)/He (Ma)
PINA	32.5628	109.7327	1,337	27.5 ± 1.0					
ASH-1A	32.7588	109.8769	1,556	54.9 ± 1.5[a]		22.5–19[b]	13.3 ± 0.7	18.1 ± 1.5	11.6 ± 0.9
SS-20-04	32.7556	109.8795	1,598	1,116 ± 19[a]			14.7 ± 3.5	25.1 ± 2.9	6.4 ± 2.6
SS-20-06	32.7545	109.8795	1,623	56.1 ± 2.1[a]	24.8 ± 1.1	22.4 ± 0.5	13.8 ± 1.6	21.6 ± 2.5	13.2 ± 4.3
SS-20-08	32.6489	109.8599	2,779	1,445 ± 6[a]			20.6 ± 1.3	21.2 ± 1.7	22.5 ± 3.8
SS-20-09	32.7329	109.8264	1,862	1,443 ± 4[a]	33.9 ± 1.4				
SS-20-10	32.7352	109.8310	2,095	1,456 ± 6[a]			20.5 ± 1.4	23.9 ± 1.8	17.0 ± 2.0

Note. Zircon U-Pb dates are weighted means of concordant analyses ±2σ. $^{40}Ar/^{39}Ar$ data are reported as integrated gas dates ±2σ. Apatite fission-track data are presented as the central age ±1σ. Zircon and apatite (U-Th)/He dates are presented as the weighted mean date ±2σ. [a]Crystallization ages presented in Scoggin, Chapman, et al. (2021). [b]Sample yields a cooling spectra and is not described by a single date.

3.2. Apatite and Zircon (U-Th)/He Thermochronology

Apatite (U-Th-Sm)/He (AHe) and zircon (U-Th)/He (ZHe) analyses were performed at the University of Arizona Radiogenic Helium Dating Laboratory following the procedures of Reiners et al. (2004) (Figure 5). Apatite and zircon grains were measured and packed into 1-mm Nb tubes, then placed into a copper planchet for degassing. Single crystal aliquots were degassed by diode or CO_2 lasers in a high vacuum extraction line at temperatures in the range of 1100–1250°C for 15-min extraction intervals, and subsequently re-extracted at higher laser power and temperature until He yields were below 2%–3% of the total. Gas extractions were measured relative to a ^{3}He spike on a quadrupole mass spectrometer. Relevant standards include Durango apatite (date range = 32.2–31.2 Ma) and Fish Canyon Tuff zircon (date range = 30.9–26.7 Ma). After degassing, apatite and zircon grains were dissolved and parent nuclide concentrations were measured by isotope dilution with a ^{233}U-^{239}Th spike on a Thermo Fisher Element2 SC-ICP-MS. Alpha ejection corrections for unknown (U-Th)/He aliquots were applied following the equations presented in Farley and Stockli (2002) and Hourigan et al. (2005) for apatite and zircon, respectively. Grain dimensions and grain shape were recorded to apply an age correction (Farley et al., 1996).

3.3. Apatite Fission-Track Thermochronology

Apatite fission-track ages were determined using the external detector method (Gleadow & Lovering, 1977; Wagner & Van den Haute, 2012). Apatite crystals were mounted in epoxy and polished to expose the interior of the crystals, and spontaneous fission tracks were revealed after etching in 5.5 M HNO_3 for 20 s at 21°C (Donelick et al., 2005). Aliquots were irradiated at the Oregon State University TRIGA reactor. The neutron fluence during irradiation was monitored using CN5 U-doped glass (Bellemans et al., 1995). After irradiation, external mica prints were etched in 40% HF for 45 min at 21°C. Fission-track analyses were performed by G. Jepson at the University of Arizona Fission-Track Laboratory using an Olympus optical microscope at 1,600X magnification with a drawing tube located above a digitizing tablet and a Kinetek computer-driven stage controlled by the FT Stage program provided by Trevor Dumitru. The central ages were calculated using the ζ-method of Hurford and Green (1983).

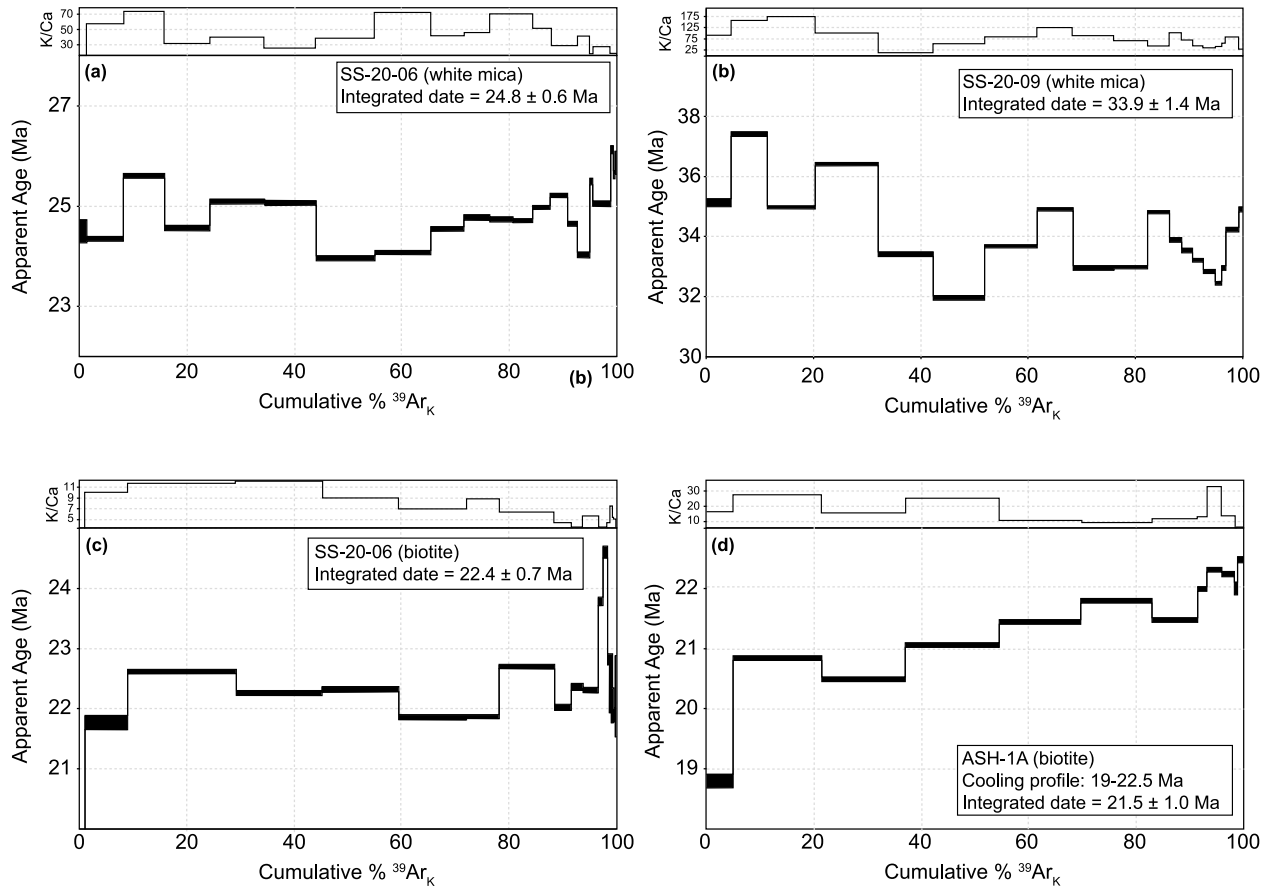

Figure 4. Apparent-age spectra and K/Ca values for biotite and white mica $^{40}Ar/^{39}Ar$ analyses. See text for interpretation of dates.

3.4. Thermal History Modeling

Thermochronologic data were initially inverse modeled using HeFTy software v.1.9.3 (Ketcham, 2005) to investigate time-temperature histories. Two thermal history models are presented (Figure 6). The first uses data from samples clustered in the Ash Creek Canyon area (Figure 3) that are located at relatively low elevation (~1,600 m). The "low elevation model" includes data from samples ASH-1A, SS-20-04, and SS-20-06 from this study and samples PM-3 and PM-4 from Long et al. (1995) (Figure 6a). A second, "high elevation model" (>1,800 m) is presented using data from samples SS-20-08, SS-20-09, and SS-20-10 (Figure 6b). Both HeFTy models employ a synthetic grain approach, where input grains are calculated from binned and averaged AHe and ZHe grains (Figure 6). No exploration boxes (cf. Murray et al., 2022) were used to further constrain the HeFTy inverse models, so all results represent monotonic cooling histories without reheating. The relatively narrow range of time investigated is interpreted to be dominated by tectonic exhumation and cooling. Full details on the modeling are presented in Supporting Information S1 (Table S1) and discussed below.

The time-temperature path from the HeFTy inverse model for the low-elevation samples was refined using radiation damage accumulation and annealing models (RDAAM) for zircon (Guenthner, 2021; Guenthner et al., 2013) and apatite (Flowers et al., 2009) (U-Th)/He data. The results of ZHe and AHe RDAAM modeling are presented together, although data was modeled separately using the respective, zircon or apatite, RDAAM model. RDAAM models are forward models that take user-defined time-temperature histories and output hypothetical single grain dates for a range of effective uranium content (eU) and effective spherical radius (Rs) values that can be compared with real data. The RDAAM models produced include a Best Fit Model, Forward Model 1, and Forward Model 2 (Figures 5 and 6), discussed below.

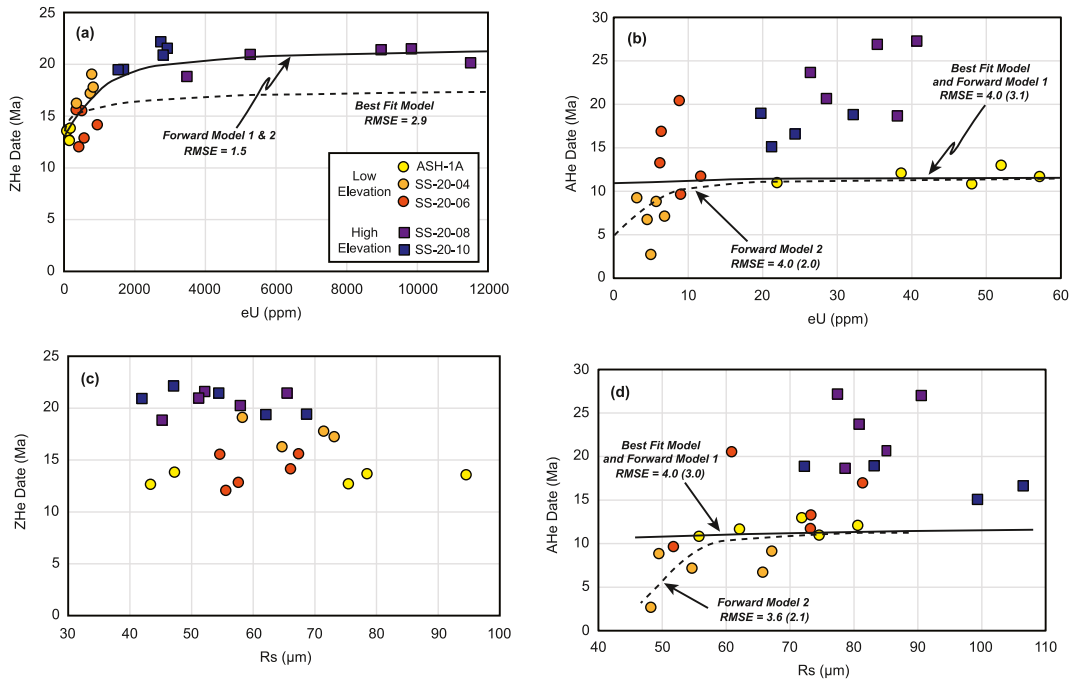

Figure 5. Summary of zircon and apatite (U-Th)/He data. Error bars are equal to or smaller than the symbol. Best-Fit Model, Forward Model 1, and Forward Model 2 are forward models that use radiation damage accumulation and annealing models for zircon (Guenthner, 2021; Guenthner et al., 2013) and apatite (Flowers et al., 2009). Time-temperature paths for each forward model are shown in Figure 6. (a) ZHe date versus eU (effective uranium concentration). Root mean square error (RMSE) is reported between models and all data. (b) AHe date versus eU. RMSE is reported between models and all low-elevation data. Values in parentheses are RMSE when the three oldest (>13 Ma) gains are excluded. (c) ZHe date versus Rs (effective spherical radius). (d) AHe versus Rs. RMSE is reported the same as in panel b.

4. Results

4.1. Muscovite and Biotite $^{40}Ar/^{39}Ar$ Thermochronology

$^{40}Ar/^{39}Ar$ incremental heating data are presented in Figure 4 and in Supporting Information S1 (Table S2). Samples were heated using a laser during analysis and no temperature data are available to create Arrhenius plots. Because of the high precision of the analyses, none of the samples can be considered true age plateaus, however, apparent ages for heating steps generally vary by <3 Myr for each sample. For this reason, we report weighted mean integrated dates ("total gas" or "total fusion"), for each sample and calculate uncertainty at 2σ, by adding in quadrature the average step apparent age uncertainty and the standard deviation of individual steps for each sample. This is a conservative uncertainty estimate and helps to more faithfully capture the full range of dates from heating steps in the reported uncertainty.

The age spectrum for white mica sample SS-20-06 varies from 24 to 26 Ma (Figure 4a). Apparent age increases over the last 50% of cumulative $^{39}Ar_K$ released, which could be considered a cooling profile. $^{40}Ar/^{36}Ar$ for this sample is atmospheric and the sample has an integrated date of 24.8 ± 0.6 Ma. The age spectrum for white mica sample SS-20-09 chiefly varies from 33 to 37 Ma, shows no systematic changes in apparent age with cumulative $^{39}Ar_K$ released, and has an integrated date of 33.9 ± 1.4 Ma (Figure 4b). $^{40}Ar/^{36}Ar$ for sample SS-20-09 is higher than atmospheric (333), but the inverse isochron date, 33.7 ± 2.5 Ma (2σ), overlaps with the integrated date. The age spectrum for biotite sample SS-20-06 chiefly varies from 21.5 to 23 Ma (Figure 4c). Apparent age steps rapidly increased over the first 30% of cumulative $^{39}Ar_K$ released, remained stable between 30% and 60%, and was variable over the last 40% with a variable release pattern for the last high-T steps. $^{40}Ar/^{36}Ar$ for this sample is atmospheric and the sample has an integrated date of 22.4 ± 0.7 Ma, excluding the first heating step (<1% of cumulative $^{39}Ar_K$). The age spectrum from biotite sample ASH-1A yields a cooling profile from 22.5 to 19 Ma, which encompasses >99.9% of the cumulative $^{39}Ar_K$ released (Figure 4d). $^{40}Ar/^{36}Ar$ for this sample is sub-

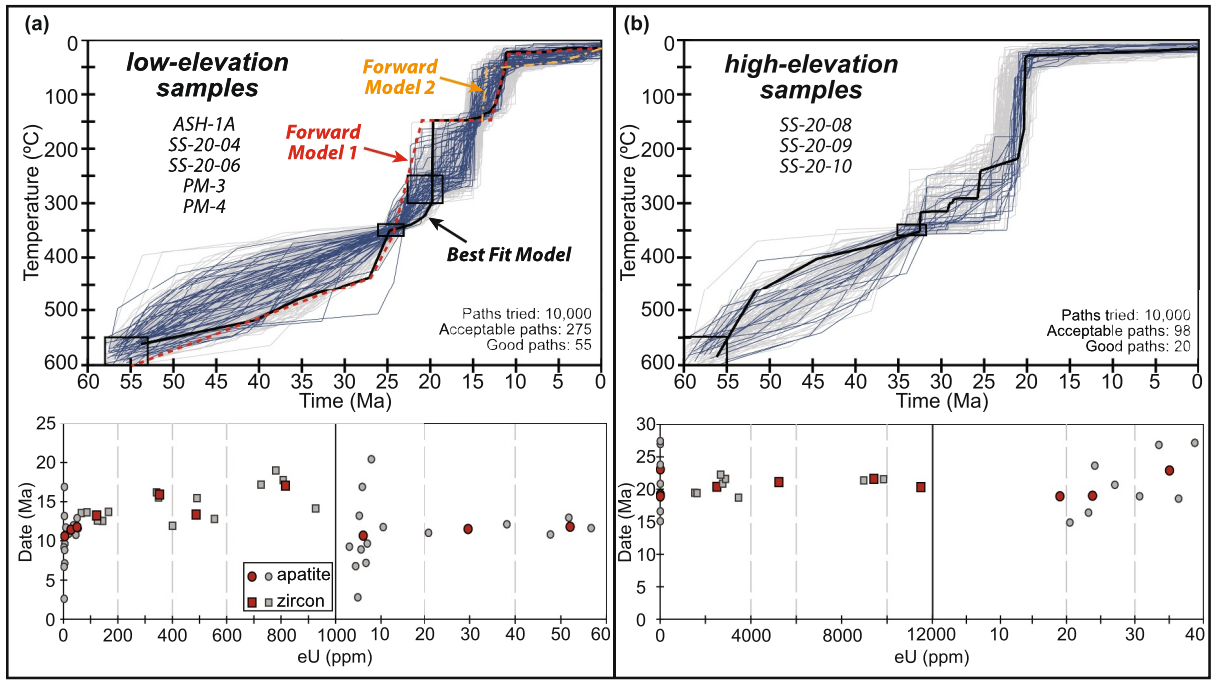

Figure 6. Time-temperature (T-t) inversion models generated in HeFTy 1.9.3 (Ketcham, 2005) using AHe and ZHe data as inputs and biotite $^{40}Ar/^{39}Ar$, white mica $^{40}Ar/^{39}Ar$, and the zircon U-Pb crystallization age of the Relleno Suite as constraints (black boxes). (a) Low-elevation samples (ca. 1,600 m) and (b) high-elevation samples (>1,800 m) are modeled separately. Lower panels show AHe (circles) and ZHe (squares) date-eU data (gray points) and averages binned (gray vertical lines) by eU (red points).

atmospheric (266) and yields an integrated date of 21.5 ± 1.0 Ma, although the apparent age steps are better interpreted as a cooling profile.

4.2. Apatite and Zircon (U-Th)/He Thermochronology

Individual grain ZHe dates from five samples range from 22.1 to 12.1 Ma (Table 2). Full details are presented in Supporting Information S1 (Table S3). Samples SS-20-04, SS-20-08, and SS-20-10 display positive date-effective Uranium (eU) trends while aliquots from samples ASH-1A and SS-20-06 have relatively restricted eU values (Figure 5a). Samples ASH-1A, SS-20-04, and SS-20-06 display eU concentrations that range from 67 to 930 ppm and ZHe dates of 19–10 Ma (Figure 5a). Sample SS-20-08 and SS-20-10 display a much larger eU spread of 1,574–11,500 ppm and ZHe dates of 22–19 Ma (Figure 5a). Trends were identified visually and then later quantified with inverse and forward modeling (see Discussion section) using root mean square error (RMSE) as a measure of goodness of fit. All samples show relatively consistent ZHe dates relative to Rs, indicating that grain size was most likely not a dominant control on ZHe dates (Figure 5c).

Individual grain AHe dates of five samples range from 27.0 to 2.7 Ma (Table 2). Full details are presented in Supporting Information S1 (Table S4). eU values for all samples are relatively restricted such that possible AHe date-eU trends are not readily apparent, although sample ASH-1A shows consistent AHe dates from eU values ranging from 22 to 57 ppm (Figure 5b). Similar to the ZHe data from these rocks, samples ASH-1A and SS-20-04 record the youngest dates but display a range of eU concentrations in the range 3–57 ppm. Sample SS-20-06 yields slightly older dates in the range 20.6–9.7 Ma but displays eU concentrations in the range 6–12 ppm. Samples SS-20-08 and SS-20-10 record the oldest AHe dates from the range of 27.3–15.0 Ma and eU concentrations of 20–41 ppm. All samples show weak to no AHe versus Rs trends, which might be a result of the limited range in AHe date for most samples (Figure 5d).

4.3. Apatite Fission-Track Thermochronology

AFT results are reported as the central age ± 1σ uncertainty. Complete fission-track data are presented in Supporting Information S1 (Table S5). Central ages of five apatite fission-track samples range from 25.1 ± 2.9 to

Table 2
Chemical, Dimensional, and (U-Th)/He Data for Samples in This Study

Sample/aliquot	nmol He ± 1s (%)	ng U ± 1s (%)	ng Th ± 1s (%)	eU (ppm)	Rs (μm)	Date ± 1σ (Ma)	WMD ± 2σ (Ma)
Apatite (U-Th)/He							
ASH-1A_a1	22.01 ± 0.3	0.28 ± 1.5	0.50 ± 1.5	51.9	71.8	13.0 ± 0.1	11.6 ± 0.9
ASH-1A_a2	7.49 ± 0.4	0.11 ± 1.4	0.21 ± 1.5	21.9	74.5	11.0 ± 0.1	
ASH-1A_a3	12.22 ± 0.4	0.18 ± 1.5	0.31 ± 1.4	57.1	62.1	11.7 ± 0.1	
ASH-1A_a4	6.69 ± 0.4	0.11 ± 1.5	0.21 ± 1.5	48.0	55.7	10.8 ± 0.1	
ASH-1A_a5	21.93 ± 0.4	0.26 ± 1.4	0.64 ± 1.5	38.6	80.6	12.1 ± 0.1	
SS-20-04_a1	0.13 ± 5.0	0.01 ± 2.1	0.01 ± 4.0	5.0	48.2	2.7 ± 0.1	6.4 ± 2.6
SS-20-04_a2	0.69 ± 2.2	0.02 ± 1.6	0.03 ± 1.5	6.8	54.6	7.2 ± 0.2	
SS-20-04_a3	0.72 ± 1.7	0.01 ± 1.8	0.03 ± 1.6	3.1	67.1	9.2 ± 0.2	
SS-20-04_a4	0.56 ± 2.6	0.01 ± 1.7	0.02 ± 1.5	5.7	49.4	8.9 ± 0.3	
SS-20-04_a5	0.55 ± 1.2	0.01 ± 1.7	0.02 ± 1.5	4.5	65.7	6.8 ± 0.1	
SS-20-06_a1	4.32 ± 0.4	0.06 ± 1.5	0.09 ± 1.5	11.7	73.2	11.8 ± 0.1	13.2 ± 4.3
SS-20-06_a2	2.82 ± 0.7	0.04 ± 1.5	0.03 ± 1.5	6.1	73.2	13.3 ± 0.2	
SS-20-06_a3	6.35 ± 0.4	0.07 ± 1.5	0.04 ± 1.5	6.3	81.4	16.9 ± 0.2	
SS-20-06_a4	3.53 ± 0.5	0.04 ± 1.5	0.02 ± 1.6	8.9	60.9	20.6 ± 0.3	
SS-20-06_a5	0.93 ± 1.0	0.02 ± 2.2	0.02 ± 1.5	8.9	51.7	9.7 ± 0.2	
SS-20-08_a1	36.46 ± 0.3	0.25 ± 1.5	0.37 ± 1.5	26.3	80.8	23.8 ± 0.3	22.5 ± 3.8
SS-20-08_a2	72.39 ± 0.2	0.43 ± 1.5	0.66 ± 1.5	35.3	90.5	27.0 ± 0.3	
SS-20-08_a3	45.01 ± 0.2	0.27 ± 1.4	0.43 ± 1.5	40.7	77.3	27.3 ± 0.3	
SS-20-08_a4	25.69 ± 0.3	0.22 ± 1.5	0.39 ± 1.5	37.9	78.5	18.7 ± 0.2	
SS-20-08_a5	31.30 ± 0.3	0.24 ± 1.5	0.40 ± 1.4	28.5	85.0	20.8 ± 0.2	
SS-20-10_a1	41.75 ± 0.2	0.49 ± 1.4	0.19 ± 1.5	24.3	106.4	16.6 ± 0.2	17.0 ± 2.0
SS-20-10_a2	9.31 ± 0.4	0.11 ± 1.5	0.01 ± 1.5	19.8	72.1	18.9 ± 0.3	
SS-20-10_a3	24.23 ± 0.3	0.26 ± 1.5	0.09 ± 1.5	32.1	83.2	18.9 ± 0.3	
SS-20-10_a4	22.25 ± 0.3	0.31 ± 1.4	0.03 ± 1.6	21.4	99.4	15.0 ± 0.2	
Zircon (U-Th)/He							
ASH-1A_z1	104.87 ± 0.2	1.49 ± 1.6	0.85 ± 1.5	88.5	78.5	13.7 ± 0.2	13.3 ± 0.7
ASH-1A_z2	93.83 ± 0.3	1.46 ± 1.5	0.76 ± 1.5	126.9	75.4	12.7 ± 0.2	
ASH-1A_z3	144.16 ± 0.3	1.97 ± 1.5	1.28 ± 1.5	67.4	94.5	13.6 ± 0.2	
ASH-1A_z4	18.42 ± 0.4	0.32 ± 1.5	0.22 ± 1.5	145.4	43.3	12.7 ± 0.2	
ASH-1A_z5	25.50 ± 0.5	0.39 ± 1.5	0.31 ± 1.5	167.5	47.2	13.8 ± 0.2	
SS-20-04_z1[a]	480.13 ± 0.2	10.90 ± 1.5	0.94 ± 1.5	2,728.9	58.2	10.2 ± 0.2	14.7 ± 3.5
SS-20-04_z2	482.10 ± 0.2	5.38 ± 1.5	3.00 ± 1.5	809.0	74.4	17.8 ± 0.2	
SS-20-04_z3	265.47 ± 0.2	2.79 ± 1.5	2.10 ± 1.5	781.4	58.3	19.1 ± 0.2	
SS-20-04_z4	397.27 ± 0.3	4.39 ± 1.5	3.25 ± 1.5	729.0	73.2	17.3 ± 0.2	
SS-20-04_z5	127.77 ± 0.3	1.54 ± 1.5	1.12 ± 1.5	343.9	64.6	16.3 ± 0.2	
SS-20-06_z1	234.80 ± 0.7	3.12 ± 1.5	1.26 ± 1.5	351.2	67.3	15.6 ± 0.2	13.8 ± 1.6
SS-20-06_z2	113.02 ± 0.4	1.58 ± 1.5	0.66 ± 1.5	493.1	54.5	15.6 ± 0.2	
SS-20-06_z3	133.03 ± 0.1	2.27 ± 1.5	0.67 ± 1.5	556.5	57.5	12.9 ± 0.2	
SS-20-06_z4	489.61 ± 0.1	7.54 ± 1.5	1.35 ± 1.6	928.9	66.1	14.2 ± 0.2	
SS-20-06_z5	76.18 ± 0.2	1.38 ± 1.6	0.54 ± 1.5	402.6	55.4	12.1 ± 0.2	
SS-20-08_z1	5,147.31 ± 0.2	57.19 ± 1.5	10.14 ± 1.9	115,500.1	57.9	20.3 ± 0.3	20.6 ± 1.3

Table 2
Continued

Sample/aliquot	nmol He ± 1s (%)	ng U ± 1s (%)	ng Th ± 1s (%)	eU (ppm)	Rs (μm)	Date ± 1σ (Ma)	WMD ± 2σ (Ma)
SS-20-08_z2	7,633.79 ± 0.2	79.15 ± 1.5	7.91 ± 1.5	8,959.5	65.5	21.5 ± 0.3	
SS-20-08_z3	1,285.35 ± 0.2	14.30 ± 1.5	2.40 ± 1.6	5,264.2	51.1	21.0 ± 0.3	
SS-20-08_z4	661.12 ± 0.2	8.63 ± 1.5	0.95 ± 1.5	3,460.1	45.1	18.9 ± 0.3	
SS-20-08_z5	2,662.78 ± 0.2	28.67 ± 1.5	4.47 ± 1.7	9,822.7	52.2	21.7 ± 0.3	
SS-20-10_z1	433.09 ± 0.2	5.33 ± 1.5	0.24 ± 1.6	2,785.3	42.0	20.8 ± 0.3	20.5 ± 1.4
SS-20-10_z2	904.47 ± 0.2	10.60 ± 1.5	0.97 ± 1.5	1,573.7	62.0	19.3 ± 0.3	
SS-20-10_z3	1,145.45 ± 0.4	12.65 ± 1.5	0.48 ± 1.5	2,904.5	54.4	21.4 ± 0.3	
SS-20-10_z4	1,025.12 ± 0.4	11.85 ± 1.5	0.68 ± 1.5	1,673.8	68.6	19.3 ± 0.3	
SS-20-10_z5	666.89 ± 0.4	7.41 ± 1.5	0.45 ± 1.5	2,734.8	47.1	22.1 ± 0.3	

Note. Aliquot dates are α-ejection corrected and the weighted mean date (WMD) was calculated from a weighted average of aliquot dates. eU = effective uranium content; Rs = effective spherical grain radius, equivalent to R_{FT} in Flowers, Zeitler, et al. (2023). [a]Low Th/U.

18.1 ± 1.5 Ma. Apatite fission-track results yields a unimodal date distribution centered at ca. 21 Ma, and the central ages mostly overlap within error of each other except for samples SS-20-04 and ASH-1A. The χ^2 test was applied to assess whether the single-grain counts represent variation around a common mean (Galbraith, 2005). The P(χ^2) value is >0.05 for all five samples, which suggests that there is a consistent ratio of spontaneous to induced tracks and that their single-grain date distributions are representative of a single age population. Sample ASH-1A and SS-20-06 yield central ages of 18.1 ± 1.5 Ma ($\chi^2 = 13.7$) and 21.6 ± 2.5 Ma ($\chi^2 = 2.7$). Sample SS-20-04 yields a central age of 25.1 ± 2.9 Ma ($\chi^2 = 9.0$). Samples SS-20-08 and SS-20-10 yield central ages of 21.2 ± 1.7 Ma ($\chi^2 = 10.5$) and 23.9 ± 1.8 Ma ($\chi^2 = 8.7$). All samples except SS-20-08 display ZHe/AFT date inversions.

4.4. Thermal History Modeling

All low-elevation samples were collected in close proximity with no fault separation. These three samples likely experienced a near-identical thermal history and are grouped together to produce an inverse HeFTy model that takes advantage of a wider range in eU values (cf., Murray et al., 2022). The "low-elevation" model uses AHe and ZHe data as inputs and biotite and white mica $^{40}Ar/^{39}Ar$ data as constraints (Figure 6a, Table S1 in Supporting Information S1). The resulting model shows a two-stage cooling history. The first pulse in cooling is from ca. 27 to 19 Ma and predominantly reflects the $^{40}Ar/^{39}Ar$ data constraints. A second pulse of rapid cooling is constrained by AHe and ZHe data and occurred from ca. 13 to 11 Ma and brought the sample to near-surface temperatures.

The "high-elevation" HeFTy inverse model uses AHe and ZHe data from samples SS-20-08 and SS-20-10 as inputs and is constrained by white mica $^{40}Ar/^{39}Ar$ data from sample SS-20-09 (Figure 6b). Samples SS-20-09 and SS-20-10 were collected in close proximity to one another and likely experienced a near-identical thermal history. Sample SS-20-08 was collected ~10 km away from the other samples and yielded nearly identical ZHe dates, but slightly older AHe dates. ZHe and AHe data from sample SS-20-08 were included in the high-elevation HeFTy model. In contrast to the two-stage cooling history preserved at lower elevations, the high-elevation thermal history model shows a single pulse of rapid cooling from ca. 23 to 19 Ma which cooled the sample to near-surface temperatures. This cooling overlaps in time with the initial stage of cooling observed in the low-elevation model.

5. Discussion

5.1. Thermochronologic Date Populations and Exhumation of the Pinaleño Metamorphic Core Complex

AFT central ages for all samples range from 25 to 18 Ma and single grain analyses define a unimodal date population centered on ca. 22 Ma. Conversely, white mica $^{40}Ar/^{39}Ar$ dates, ZHe single grain dates, and AHe single grain dates display bimodal populations, with older dates obtained from high elevation samples (>1,800 m) (Figures 4, 7c, and 7d). Biotite $^{40}Ar/^{39}Ar$ data was not collected from high-elevation samples. Relatively older thermochronologic dates located at higher elevations in core complexes can be used to constrain exhumation rate (e.g., Foster & John, 1999). However, the ZHe and AHe data also show date-eU and date-Rs trends (Figure 5) that could explain the range in ages (e.g., Reade et al., 2020). To test for this possibility, we used RDAAM forward

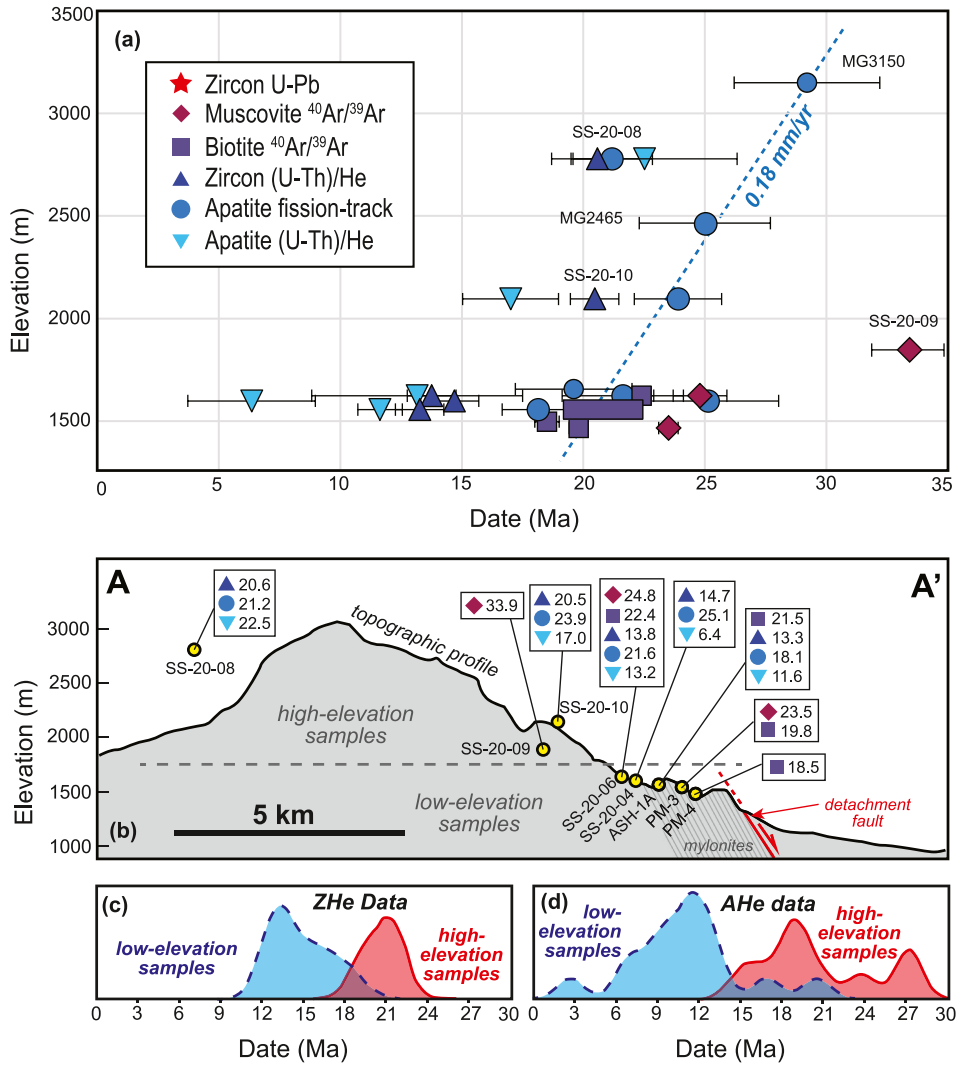

Figure 7. (a) Sample elevation versus date plot of thermochronology data from the Pinaleño Mountains. Blue dashed line is an apparent exhumation rate based on apatite fission track data, excluding sample SS-20-08. (b) Sample locations projected onto a topographic profile (~2.5× vertical exaggeration) from cross-section A-A' (location in Figure 3) showing thermochronologic dates. Normalized kernel density estimates for (c) ZHe data and (d) AHe data show that low-elevation samples have younger age populations than high-elevation samples.

modeling of zircon (Guenthner, 2021; Guenthner et al., 2013) (Figures 5a and 5c) and apatite (Flowers et al., 2009) (Figures 5b and 5d).

Our initial forward model using RDAAM uses the "best-fit" time-temperature path from the low-elevation HeFTy inverse model (Figure 6a). Unsurprisingly, the model, referred to as the Best Fit Model, performs poorly (RMSE = 2.9) at matching ZHe-eU data from high-elevation samples (Figure 5a). The model consistently predicts younger ZHe dates than are observed for the highest eU values. Previous studies of positive ZHe date-eU trends demonstrated that the increase in date for low eU values (e.g., <2,000 ppm) is particularly sensitive to the length of time that samples spend in the ZHe partial retention zone (ca. 100–180°C for moderate eU, Guenthner et al., 2013; Reiners & Brandon, 2006). The "best-fit" time-temperature path from the low-elevation HeFTy inverse model indicated nearly isothermal conditions (~150°C) within the ZHe partial retention zone from 20 to 13 Ma (Figure 6a). Slightly extending the isothermal period to 21–13 Ma (Figure 6a), referred to as Forward Model 1, produces a better match (RMSE = 1.5) to the ZHe-eU data (Figure 5). These results are not a "best-fit" or inverse model and our modeling philosophy was to make minimal adjustments to the original HeFTy model to better fit the data.

Forward Model 1 suggests relatively constant, rapid cooling (30–60°C/Myr) from 27 to 21 Ma. The main difference between Forward Model 1 and the Best Fit Model is the inclusion of biotite $^{40}Ar/^{39}Ar$ data as a constraint in the Best Fit Model. Forward Model 1 predicts biotite $^{40}Ar/^{39}Ar$ dates that are up to 4 Myr older than observed. We do not prefer one model over another, and it is unclear whether biotite $^{40}Ar/^{39}Ar$ data should be weighted more or less than (U-Th)/He data. It is worth noting that the Best Fit Model indicates very rapid cooling (>300°C/Myr) at ca 21 Ma, which may be geologically unrealistic. Cooling rates associated with exhumation of the North American metamorphic core complexes generally do not exceed 100°C/Myr (see review in Whitney et al. (2013)). Regardless, the differences between the Best Fit Model and Forward Model 1 are relatively minor and overall indicate an initial period of rapid cooling during 27–21 Ma, a nearly isothermal period during 21–13 Ma, and a second period of rapid cooling during 13–11 Ma. The onset of rapid cooling is ≥25 Ma based on white mica $^{40}Ar/^{39}Ar$ dates from this study and Long et al. (1995), but remains poorly constrained. We estimate the onset of cooling at ∼27 Ma based on the range of good paths in the low-elevation HeFTy model.

We interpret the initial period of rapid cooling (∼27–21 Ma) as the timing of exhumation for the Pinaleño metamorphic core complex that was accomplished by displacement across the mylonitic shear zone and detachment fault. This period of cooling, from ∼450 to 150°C, is consistent with quartz microstructures in Pinaleño mylonitic rocks that exhibit dynamic recrystallization (Bailey & Eyster, 2003; Naruk, 1986) and encompasses the brittle-ductile transition. The onset of rapid cooling is interpreted to indicate the onset of extensional deformation.

Forward Model 1 (Figure 5a) indicates that the bimodal distribution of single grain ZHe dates (Figure 7c) can be explained by radiation damage and annealing processes in grains with variable eU. Several 10s of forward models using RDAAM were attempted to explain the bimodal distribution of AHe dates, however, no time-temperature history was found that can match both the low-elevation and high-elevation data (Figure 5b). As a result, we interpret the multiple AHe date populations (Figure 7d) to reflect actual differences in cooling history between the low-elevation and high-elevation samples.

The higher temperature (>200°C) history for the high-elevation HeFTy inverse model is poorly constrained (single white mica $^{40}Ar/^{39}Ar$ date), but the lower temperature history (<200°C) is well constrained and indicates rapid cooling (50–80°C/Myr) during 22–20 Ma (Figure 6b). This age range overlaps with the initial period of rapid cooling in the low-elevation HeFTy model and demonstrates that the higher-elevation, structurally higher, samples were cooling through a lower temperature window (200–50°C) at the same time that the lower-elevation, structurally lower, samples were cooling through a higher temperature window (300–150°C). These temperature ranges are too broad to calculate meaningful exhumation rates, but more precise rates can be estimated by combining AFT data from this study with AFT data from Jepson et al. (2021) in an age-elevation plot along a SW-NE transect (Figure 7b). Sample MG1655 (Jepson et al., 2021), ASH-1A, SS-20-04, and SS-20-06 (this study) are all located at ∼1,600 m elevation near one another. The average AFT central age of these samples is 20.5 ± 3.8 Ma (2σ) with uncertainty calculated by adding standard deviation and average uncertainty in quadrature. Higher elevation AFT samples include MG3150, MG2465 (Jepson et al., 2021) and SS-20-10. Sample SS-20-08 was not included because it is located southwest of the main sample transect (Figure 7b). Based on AFT samples alone, the Pinaleño metamorphic core complex has an apparent exhumation rate of 0.18 mm/yr during 29–21 Ma, which is comparable to the apparent exhumation rate for the Catalina metamorphic core complex (0.24 mm/yr during 25–19 Ma, Jepson et al., 2022). This rate is an apparent rate in part because the amount of tilting and/or rotation that the Pinaleño Mountains experienced during tectonic exhumation is unknown.

5.2. Miocene Cooling: Basin and Range Extension

Almost all mylonitic shear zones and detachment faults associated with metamorphic core complexes in southern Arizona are cross-cut at a high angle to displacement direction by brittle normal faults that produce the present-day Basin and Range topography of the region, indicating a relative sequence of events (Spencer et al., 2001). However, cooling related to tectonic exhumation associated with Basin and Range-style normal faulting is rarely distinguished from tectonic exhumation associated with core complex development in thermochronologic data sets (e.g., Carter et al., 2004, 2006; Fitzgerald et al., 1993; Gottardi et al., 2020; Pease et al., 1999; Prior et al., 2016; Singleton et al., 2014). A common explanation for this is that the amount of tectonic exhumation during Basin and Range-style normal faulting may be too low to be recorded by thermochronometers (see Discussion in Foster et al. (1993)). An exception is the Catalina metamorphic core complex, located adjacent to

the Piñaleno core complex (Figure 1), from which Jepson et al. (2022) identified a transition from core complex style exhumation to Basin and Range style exhumation at ca. 17 Ma. A difference between the reconstructed time-temperature history for the Catalina metamorphic core complex and the time-temperature histories modeled for the Pinaleño core complex is that the Pinaleño Mountains experienced two distinct periods of rapid cooling (27–21 and 13–11 Ma) separated by a near-isothermal period (21–13 Ma) whereas the Catalina core complex exhibits a smooth transition from core complex-style exhumation to Basin and Range-style extension (Figure 6).

The younger period of cooling in the Pinaleño Mountains is recorded by ZHe and AHe data from low-elevation samples and is not observed in ZHe or AHe data from high-elevation samples (Figure 7). The high-elevation HeFTy model suggests that the high-elevation samples were exhumed through the ZHe and AHe closure temperature windows during the older (27–21 Ma) cooling period, interpreted to represent core complex exhumation, and have remained at the near-surface since that time. The low-elevation HeFTy model suggests that the low-elevation samples were exhumed to the near-surface in Miocene time and implies that the high-elevation samples experienced rock uplift, with minimal erosion or cooling during the Miocene. Forward modeling using RDAAM indicates that the nearly isothermal (~150°C) period from ca. 21 to 13 Ma followed by rapid cooling during 13–11 Ma can explain the positive ZHe date-eU trend and that the timing of rapid cooling is the chief control on the date of the lowest eU zircons (<200 ppm) (Figure 5a). ZHe data from this study is generally insensitive to temperatures <100°C, but AHe data can be used to further investigate the youngest part of the time-temperature history.

Low-elevation AHe data has a positive date-Rs trend and no statistically significant date-eU trend. However, if the three oldest (>13 Ma) single apatite grains from the low-elevation samples are ignored, the AHe data shows a positive date-eU trend. We modeled all low-elevation data and a data set that excluded the three oldest grains for comparison. We were able to more closely match the AHe date-Rs and AHe date-eU trends with RDAAM modeling, referred to as Forward Model 2, by making the onset of rapid Miocene cooling slightly older (13.5 Ma) and the magnitude of cooling slightly lower (Figure 6a). Decreasing the magnitude of cooling extends the time the sample spends in the He partial retention zone and causes low eU and low Rs grains to yield younger ages (Flowers, Ketcham, et al., 2023). For the Best Fit Model, RMSE = 4.0 for all low-elevation AHe-eU data and AHe-Rs data. RMSE decreases to 3.1 (AHe-eU) and 3.0 (AHe-Rs) when the three oldest grains are excluded. For Forward Model 2, RMSE = 4.0 for all low-elevation AHe-eU data and RMSE = 3.6 for low-elevation AHe-Rs data. RMSE decreases to 2.0 (AHe-eU) and 2.1 (AHe-Rs) when the oldest grains are excluded. Regardless of the exclusion of grains, Forward Model 2 provides a marginally better fit to the data than the other models and is our preferred interpretation of the time-temperature history of the low-elevation samples. Forward Model 2 could be considered an overinterpretation of the data, but the results only marginally extend our estimates for the timing of rapid Miocene cooling, from 13–11 Ma (Best Fit Model and Forward Model 1) to 13.5–11 Ma, which is a more conservative, inclusive estimate.

We interpret the period of rapid Miocene cooling to record exhumation controlled by Basin and Range extensional faulting. Many metamorphic core complexes in southern Arizona have been overprinted by Basin and Range tectonism, including the Catalina metamorphic core complex, located ~100 km southwest of the Pinaleño core complex, that was offset by high-angle normal faults at ca. 15 Ma (Davis et al., 2004; Dickinson, 1991; Fayon et al., 2000; Jepson et al., 2022). Basin and Range tectonism in southern Arizona is characterized by relatively planar, high-angle normal faulting, horst-and-graben structures, and the formation of deep basins, which is distinct from listric to low angle detachment faulting, rotation of fault blocks, and relatively shallow and asymmetric supradetachment basins associated with core complex tectonism (Spencer et al., 2001). The transition from core complex style extension to Basin and Range style extension is recorded by reflection seismic data from the Safford Basin, located in the hangingwall of the Pinaleño detachment fault, that shows (a) a high-angle normal fault cross-cutting a low-angle detachment fault and (b) a major unconformity in the subsurface separating faulted, rotated and eroded sediments below relatively flat-lying sediments (Kruger & Johnson, 1994). The age of this unconformity is not well constrained, but was estimated to be 12–13 Ma by Eberly and Stanley (1978) based on regional correlation to basins located further west and ~17 Ma by Kruger et al. (1995) based on the age of nearby volcanic rocks that show a transition from intermediate, calc-alkaline compositions to more mafic, alkaline compositions. Seismic images from the Safford Basin show that the Pinaleño detachment fault is cross-cut by a high-angle normal fault located at the range front, which helped accommodate uplift of the Pinaleño Mountains and subsidence of the Safford Basin in Miocene time (Kruger & Johnson, 1994; Kruger et al., 1995). Scoggin, Reiners, et al. (2021) also suggested that the Pinaleño Mountains experienced exhumation and cooling

related to Basin and Range extension based on Fe-oxide (U-Th)/He (FeHe) dates from the Eagle Pass area that are distributed around ∼10 Ma.

5.3. AFT and ZHe Age Inversion

For most samples analyzed in this study, the AFT central age is older than the ZHe date (weighted mean), which is unexpected if the dates are interpreted in terms of cooling through a closure temperature window. The apparent "age-inversion" observed in this study is a long-standing issue in low-temperature thermochronometric systems and can have several explanations (Reiners, 2005). First, the AFT single-grain analyses yielded extremely low spontaneous track densities (often <5 tracks per grain, Supporting Information S1 (Table S4)). As a result, small variations in the natural Poisson distribution of spontaneous fission of ^{238}U will result in significant age variation (Galbraith, 2005). However, given that the samples yielded AFT dates which are both internally and externally consistent (Jepson et al., 2021), there is no obvious reason to exclude them.

Next, the temperature sensitivity of AHe and ZHe thermochronology is strongly influenced by degree of radiation damage, proxied via eU, and prior tectonic/thermal history. The He partial retention zone for the ZHe system (ca. 100–180°C, Reiners & Brandon, 2006) can be significantly reduced for low eU grains (<1,000 ppm) that resided in a partial retention zone for extended periods (e.g., Guenthner, 2021). Experimental studies demonstrate that apparent ZHe closure temperatures can be lower than AFT closure temperatures in these situations (Ginster et al., 2019; Guenthner et al., 2013). The HeFTy inverse models and RDAAM forward models explored in this study demonstrate that this is the case for the low-elevation ZHe dates. The youngest single grain ZHe dates (∼13 Ma) have the lowest eU and record final exhumation to the near surface during Basin and Range exhumation. The oldest single grain ZHe dates (∼19 Ma) have among the highest eU and record rapid cooling (ca. 25–21 Ma) during core complex exhumation. The oldest dates and period of rapid cooling are within uncertainty of AFT central ages for the low-elevation samples (Table 2).

High-elevation sample SS-20-08 has the highest zircon eU values (>3,000 ppm) and shows no date-eU trend (Figure 5a). The AFT central age and ZHe mean age of this sample overlap within uncertainty. High-elevation sample SS-20-10 has intermediate eU values (1,500–3,000 ppm) and shows a positive date-eU trend. RDAAM modeling suggests that only the highest eU grains from this sample (>2,000 ppm) record the period of rapid cooling, defined by the date "plateau" for high eU values in Figure 5a. The highest eU grains from sample SS-20-10 have ZHe dates (21–22 Ma) that overlap with the AFT central age within uncertainty. Questions remain about the causes of AFT-ZHe age inversion, but the inversions observed in this study can largely be attributed to variations in He diffusion and annealing kinetics that can be modeled using zircon and apatite RDAAM. Additional factors not considered include mineralogical composition, lattice growth conditions, and other variation in activation energies, which are observed experimentally, but rarely discussed in applied studies (e.g., Gautheron et al., 2020; Guenthner et al., 2013). Ultimately, leveraging both annealing and diffusion kinetics through multi-method thermochronology allows for greater resolution of the thermal evolution of the upper crust.

High-elevation, Proterozoic AFT samples reported in Jepson et al. (2021) have relatively long track lengths that suggest a single phase of rapid cooling, consistent with our high-elevation HeFTy model (Figure 6b). No confined tracks were present in the low-elevation samples investigated in this study due to large, undamaged grains with extremely low spontaneous track densities. These samples were collected from the Eocene Relleno intrusive suite or from Proterozoic rocks in close proximity to the Relleno suite that are interpreted to have experienced heating during the Eocene. Future track length analyses of low-elevation samples collected away from the Relleno suite could help further constrain and test the time-temperature histories and models presented in this study.

5.4. Plate Dynamics, Magmatism, and Core Complex Exhumation Trends

This study adds to an already extensive data set on exhumation timing for the North American Cordilleran metamorphic core complexes and can help test hypotheses for the spatiotemporal trends of core complex exhumation in the southern Basin and Range province. Subduction of the Pacific-Farallon spreading center (paleo-East Pacific Rise) beneath North America and opening of a slab window or slab gap was one of the first-proposed explanations for the onset of Cenozoic extension in the western U.S. (Atwater, 1970; Dickinson & Snyder, 1979; Severinghaus & Atwater, 1990). This concept was first applied to metamorphic core complexes by Glazner and Bartley (1984) who noted that low-angle normal faulting was oldest in southern Arizona and becomes younger to the northwest, toward the Las Vegas area in Nevada, USA and that this trend is roughly coeval

with the northward migration of the Mendocino triple junction (MTJ). There are two aspects of the "slab window" models that may have contributed to core complex formation. The first is that upwelling of asthenosphere heated and buoyed the North American plate, which may have thermally and mechanically weakened the lithosphere (e.g., Axen et al., 1993; Zuza & Cao, 2023). The second is that as the slab window grew, the length of the Pacific-North American plate transform boundary increased and stress conditions within the lithosphere transitioned from compressional to neutral or extensional (e.g., Atwater & Stock, 1998). The first idea is difficult to reconcile with studies on modern slab window widening and triple junction migration that suggest the effects are highly localized to the plate margin (e.g., Furlong & Schwartz, 2004). In addition, the effects of the slab window widening are predicted to migrate inland, whereas the onset of core complex exhumation began at locations farthest from the plate margin and migrated toward the trench in the southern U.S. Cordillera (Armstrong & Ward, 1991; Coney, 1987; Dickinson, 2002). Foundering of the Farallon slab may have produced a similar effect as a slab window (see discussion below). The second idea, that a change in stress conditions is a requirement for the onset of extension, is widely accepted, but whether core complex formation tracks the migration of triple junctions or is a function of other processes remains debated (e.g., Bahadori et al., 2022). Zuza and Cao (2023) noted that there was a poor correlation between core complex exhumation and triple junction migration in the central to northern U.S. Cordillera, but the role of plate reorganization in the southern U.S. and northern Mexico Cordillera were not considered.

To evaluate this correlation, we compared the timing of rapid exhumation of core complexes (Chapman et al., 2021) with the latitudinal position of the Mendocino and Rivera triple junctions using GPlates 2.3 (Müller et al., 2018). We used the combined rotations, reconstruction tree, and reconstructed geometries of ridges, coastlines, and plate boundaries of Müller et al. (2019) and fixed the North American plate in its current position. By fixing the North American plate, all reconstructed latitudes are relative to modern latitudes. The model suggests that the Pacific-Farallon spreading center intersected the Farallon trench at approximately 31 Ma at a latitude of ~33°N, the MTJ moved northward to ~36°N by ca. 15 Ma, and the Rivera triple junction moved southward to ~28°N by ca. 23 Ma (Figure 2). The timing for initial subduction of the spreading center is consistent with independent geologic estimates for the change in stress state from compressional to extensional in the southern Basin and Range province, which cluster around ca. 32 Ma but range from 36 to 30 Ma (Aguirre-Díaz & McDowell, 1993; Cather et al., 2004; Copeland et al., 2011; Henry et al., 1991; Price & Henry, 1984). The timing and spatial pattern of triple junction migration correlates well with the initiation of rapid exhumation recorded in the footwalls of metamorphic core complexes. The earliest (oldest) initiation of rapid exhumation occurs at 32–33°N, including the Pinaleño core complex, and migrates to the north and south at a rate comparable to the migration of the triple junctions. Nowhere does the initiation of rapid exhumation precede the passage of either triple junction at that latitude, and the initiation of rapid exhumation generally occurs ≤5 Myr after passage of the triple junctions. These results are consistent with previous studies that have emphasized the gradual transition of the North American-Pacific/Farallon plate boundary from a compressional subduction zone to a neutral or transtensional transform boundary, including the San Andreas Fault system, was a main factor in initiating Cenozoic extension in the southern U.S. and northern Mexican Cordillera (Atwater, 1970).

Another common explanation for the spatiotemporal pattern of metamorphic core complex formation in the southern Basin and Range province is that enhanced heat flow from increased asthenospheric upwelling following roll-back or foundering of the Farallon slab and magmatism associated with the mid-Cenozoic ignimbrite flare-up weakened the crust (e.g., Armstrong & Ward, 1991). At the scale of individual core complexes (≤50 km^2), there is a weak correlation between timing of extension and voluminous mid-Cenozoic flare-up volcanism (Spencer et al., 1995), but many recent data compilations at regional to orogenic scales show a close correlation between core complex exhumation and magmatism timing (Howlett et al., 2021; Konstantinou, 2022; Lund-Snee & Miller, 2022; Zuza & Cao, 2023). To further examine this relationship, we compiled geochronology data from EarthChem and plotted igneous rock ages on Figure 2. Magmatism correlates well with core complex exhumation in the southern U.S. Cordillera, although there appears to be no correlation in northern Mexico. We suspect this is an artifact due to a lack of data from this region. Another way to investigate the correlation is to compare exhumation timing to the age of intrusive rocks located within core complexes, exposed in their footwalls (Figure 2). Most metamorphic complexes in the southern Basin and Range province, including in Mexico, experienced syn-kinematic plutonism, strengthening the correlation between magmatism and core complex formation. We suspect that these plutons, including the Oligocene Goodwin Canyon quartz monzonite and Gillespie granite in the Pinaleño Mountains, are the most significant sources for added heat. Models for

conductive heating of the crust due to increased basal heat flow (e.g., asthenospheric upwelling) suggest peak crustal temperatures are not attained for up to several 10s of Myr (e.g., Bodell & Chapman, 1982), whereas heating associated with magmatic intrusions occurs at timescales of ≤1 Myr (Annen & Sparks, 2002).

There are additional hypotheses for core complex formation, including gravitational collapse of tectonically thickened crust (Bahadori et al., 2022; Chapman et al., 2020; Coney & Harms, 1984; Sonder & Jones, 1999; Spencer et al., 1995) that are important, but not addressed by the new data presented in this study. Regardless of the exact processes involved in the development of the Cordilleran core complexes in the southern Basin and Range province, we note that trench-parallel trends (e.g., the migration of triple junctions and changes in stress state) are equally important as trench-perpendicular trends (e.g., inboard and outboard magmatic sweeps) to consider.

6. Conclusions

New thermochronologic data, HeFTy inverse modeling, and forward modeling using zircon and apatite RDAAM indicate that the Pinaleño Mountains experienced two periods of rapid cooling during the Cenozoic. The first period of rapid cooling started ≥25 Ma and is estimated to have occurred during 27–21 Ma with a cooling rate of 30–60°C/Myr. This period of cooling records formation and exhumation of the Pinaleño metamorphic core complex, which had an apparent exhumation rate of 0.18 mm/yr based on AFT data from a vertical transect. Rocks at modern elevations >1,800 m are interpreted to have cooled to near surface temperatures by 21 Ma. During 27–21 Ma, rocks exposed at lower elevations in the footwall of the Pinaleño core complex cooled from >400 to ca. 150°C and remained near this temperature until ∼13.5 Ma. The Pinaleño Mountains are interpreted to have experienced little to no exhumation during 21–13.5 Ma. This protracted period of nearly isothermal temperatures within the ZHe partial retention zone resulted in the date-eU trends observed in the (U-Th)/He data.

The second period of rapid cooling occurred during 13.5 to 11 Ma and is interpreted to record tectonic exhumation associated with Basin and Range extensional faulting. This interpretation supports previous studies that recognized high-angle normal faults and sedimentary deposits related to Basin and Range extension in reflection seismic images from the Safford Basin. Rocks at modern elevations <1,800 m in the Pinaleño Mountains are interpreted to have cooled to near surface temperatures during this time and rocks at higher elevations are interpreted to have experienced rock uplift.

The timing of exhumation of the Pinaleño metamorphic core complex overlaps with other nearby core complexes, including the Catalina Mountains and Coyote Mountains core complexes (Fayon et al., 2000; Gottardi et al., 2020; Jepson et al., 2022). This indicates that core complex exhumation initiated at 32–33°N latitude in the southern Basin and Range province and migrated toward the northwest and south contemporaneously. The timing and latitude of core complex exhumation initiation correlates well with the timing and latitude of initial subduction of the Pacific-Farallon spreading ridge and the transition of the plate margin to a transform boundary. The transform boundary lengthened as the Mendocino and Rivera triple junctions migrated northward and southward, respectively, which correlates well with the spatiotemporal pattern of core complex exhumation in the southern Basin and Range province. The timing of core complex exhumation also correlates well with the timing of magmatism associated with the mid-Cenozoic flare up, including igneous rocks intruded into core complex footwalls. These observations suggest that core complex exhumation in the southern Basin and Range province resulted from a combination of interrelated processes including stress regime change, removal of the Farallon plate, and regional magmatism.

Data Availability Statement

Data and full details from biotite and white mica Ar/Ar analyses, apatite and zircon (U-Th)/He analyses, apatite fission track analyses, and details of the inverse modeling performed are available at https://doi.org/10.5281/zenodo.8186926.

Acknowledgments
Chapman acknowledges support from U.S. National Science Foundation Grant EAR-1928312. Scoggin acknowledges support from the Geological Society of America. We thank Drs. Mark Pecha, Martin Pepper, Sarah George, and Uttam Chowdhury for analytical assistance, Dr. Mike Darin and anonymous reviewers for constructive reviews, and Drs. Kevin Chamberlain and Barbara John for insightful discussion.

References

Aguirre-Díaz, G. J., & McDowell, F. W. (1993). Nature and timing of faulting and synextensional magmatism in the southern Basin and Range, central-eastern Durango, Mexico. *Geological Society of America Bulletin*, *105*(11), 1435–1444. https://doi.org/10.1130/0016-7606(1993)105<1435:natofa>2.3.co;2

Annen, C., & Sparks, R. S. J. (2002). Effects of repetitive emplacement of basaltic intrusions on thermal evolution and melt generation in the crust. *Earth and Planetary Science Letters*, *203*(3–4), 937–955. https://doi.org/10.1016/s0012-821x(02)00929-9

Arca, M. S., Kapp, P., & Johnson, R. A. (2010). Cenozoic crustal extension in southeastern Arizona and implications for models of core-complex development. *Tectonophysics*, *488*(1–4), 174–190. https://doi.org/10.1016/j.tecto.2010.03.021

Armstrong, R., & Ward, P. (1991). Evolving geographic patterns of Cenozoic magmatism in the North American Cordillera: The temporal and spatial association of magmatism and metamorphic core complexes. *Journal of Geophysical Research*, *96*(B8), 13201–13224. https://doi.org/10.1029/91jb00412

Atwater, T. (1970). Implications of plate tectonics for the Cenozoic tectonic evolution of western North America. *Geological Society of America Bulletin*, *81*(12), 3513–3536. https://doi.org/10.1130/0016-7606(1970)81[3513:ioptft]2.0.co;2

Atwater, T., & Stock, J. (1998). Pacific-North America plate tectonics of the Neogene southwestern United States: An update. *International Geology Review*, *40*(5), 375–402. https://doi.org/10.1080/00206819809465216

Axen, G. J., Taylor, W. J., & Bartley, J. M. (1993). Space-time patterns and tectonic controls of Tertiary extension and magmatism in the Great Basin of the western United States. *Geological Society of America Bulletin*, *105*(1), 56–76. https://doi.org/10.1130/0016-7606(1993)105<0056:stpatc>2.3.co;2

Bahadori, A., Holt, W. E., Austermann, J., Campbell, L., Rasbury, E. T., Davis, D. M., et al. (2022). The role of gravitational body forces in the development of metamorphic core complexes. *Nature Communications*, *13*(1), 5646. https://doi.org/10.1038/s41467-022-33361-2

Bailey, C. M., & Eyster, E. L. (2003). General shear deformation in the Pinaleño Mountains metamorphic core complex, Arizona. *Journal of Structural Geology*, *25*(11), 1883–1892. https://doi.org/10.1016/s0191-8141(03)00044-0

Bellemans, F., De, F., & Van Den, P. (1995). Composition of SRM and CN U-doped glasses: Significance for their use as thermal neutron fluence monitors in fission track dating. *Radiation Measurements*, *24*(2), 153–160. https://doi.org/10.1016/1350-4487(94)00100-f

Bodell, J. M., & Chapman, D. S. (1982). Heat flow in the north-central Colorado Plateau. *Journal of Geophysical Research*, *87*(B4), 2869–2884. https://doi.org/10.1029/jb087ib04p02869

Bright, R. M., Amato, J. M., Denyszyn, S. W., & Ernst, R. E. (2014). U-Pb geochronology of 1.1 Ga diabase in the southwestern United States: Testing models for the origin of a post-Grenville large igneous province. *Lithosphere*, *6*(3), 135–156. https://doi.org/10.1130/l335.1

Carter, T. J., Kohn, B. P., Foster, D. A., & Gleadow, A. J. (2004). How the Harcuvar Mountains metamorphic core complex became cool: Evidence from apatite (U-Th)/He thermochronometry. *Geology*, *32*(11), 985–988. https://doi.org/10.1130/g20936.1

Carter, T. J., Kohn, B. P., Foster, D. A., Gleadow, A. J., & Woodhead, J. D. (2006). Late-stage evolution of the Chemehuevi and Sacramento detachment faults from apatite (U-Th)/He thermochronometry – Evidence for mid-Miocene accelerated slip. *Geological Society of America Bulletin*, *118*(5–6), 689–709. https://doi.org/10.1130/b25736.1

Cather, S. M., Mack, G. H., & Giles, K. A. (2004). Laramide orogeny in central and northern New Mexico and southern Colorado. *The Geology of New Mexico, A Geologic History: New Mexico Geological Society Special Publication*, *11*, 203–248.

Chapman, J. B., Greig, R., & Haxel, G. B. (2020). Geochemical evidence for an orogenic plateau in the southern US and northern Mexican Cordillera during the Laramide orogeny. *Geology*, *48*(2), 164–168. https://doi.org/10.1130/g47117.1

Chapman, J. B., Runyon, S. E., Shields, J., Lawler, B. L., Pridmore, C. J., Scoggin, S. H., et al. (2021). The North American Cordilleran Anatectic belt. *Earth-Science Reviews*, *215*, 103576. https://doi.org/10.1016/j.earscirev.2021.103576

Coney, P. J. (1980). Cordilleran metamorphic core complexes: An overview. *Geological Society of America Memoir*, *153*, 7–31.

Coney, P. J. (1987). The regional tectonic setting and possible causes of Cenozoic extension in the North American Cordillera. Geological Society, London, Special Publications (Vol. *28*, pp.177–186).

Coney, P. J., & Harms, T. A. (1984). Cordilleran metamorphic core complexes: Cenozoic extensional relics of Mesozoic compression. *Geology*, *12*(9), 550–554. https://doi.org/10.1130/0091-7613(1984)12<550:cmccce>2.0.co;2

Cooper, J. R., & Silver, L. T. (1964). Geology and ore deposits of the Dragoon quadrangle. Arizona: Cochise County, U.S. Geological Survey Professional Paper (Vol. *416*).

Copeland, P., Murphy, M. A., Dupré, W. R., & Lapen, T. J. (2011). Oligocene Laramide deformation in southern New Mexico and its implications for Farallon plate geodynamics. *Geosphere*, *7*(5), 1209–1219. https://doi.org/10.1130/ges00672.1

Creasey, S. C., Banks, N. G., Ashley, R. P., & Theodore, T. G. (1977). Middle tertiary plutonism in the Santa Catalina and Tortolita Mountains, Arizona. *U.S. Geological Survey Journal of Research*, *5*, 705–717.

Davis, G. H., Constenius, K. N., Dickinson, W. R., Rodriguez, E. P., & Cox, L. J. (2004). Fault and fault-rock characteristics associated with Cenozoic extension and core-complex evolution in the Catalina-Rincon region, southeastern Arizona. *Geological Society of America Bulletin*, *116*(1), 128–141. https://doi.org/10.1130/b25260.1

Davis, G. H., & Hardy JR, J. J. (1981). The Eagle Pass detachment, southeastern Arizona: Product of mid-Miocene listric (?) normal faulting in the southern Basin and Range. *Geological Society of America Bulletin*, *92*(10), 749–762. https://doi.org/10.1130/0016-7606(1981)92<749:tepdsa>2.0.co;2

Dickinson, W. R. (1991). Tectonic setting of faulted Tertiary strata associated with the Catalina core complex in southern Arizona. Geological Society of America Special Paper (Vol. *264*).

Dickinson, W. R. (2002). The Basin and Range Province as a composite extensional domain. *International Geology Review*, *44*, 1–38. https://doi.org/10.2747/0020-6814.44.1.1

Dickinson, W. R., & Snyder, W. S. (1979). Geometry of subducted slabs related to San Andreas transform. *The Journal of Geology*, *87*(6), 609–627. https://doi.org/10.1086/628456

Dokka, R. K., & Ross, T. M. (1995). Collapse of southwestern North America and the evolution of early Miocene detachment faults, metamorphic core complexes, the Sierra Nevada Orocline, and the San Andreas fault system. *Geology*, *23*(12), 1075–1078. https://doi.org/10.1130/0091-7613(1995)023<1075:cosnaa>2.3.co;2

Donelick, R. A., O'Sullivan, P. B., & Ketcham, R. A. (2005). Apatite fission-track analysis. *Reviews in Mineralogy and Geochemistry*, *58*(1), 49–94. https://doi.org/10.2138/rmg.2005.58.3

Drewes, H. (1996). Geology of coronado national forest. *US Geological Survey Bulletin*, *2083*, 17–41.

Eberly, L. D., & Stanley, T. B., Jr. (1978). Cenozoic stratigraphy and geologic history of southwestern Arizona. *Geological Society of America Bulletin*, *89*(6), 921–940. https://doi.org/10.1130/0016-7606(1978)89<921:csagho>2.0.co;2

Farley, K. A., & Stockli, D. F. (2002). (U-Th)/He dating of phosphates: Apatite, monazite, and xenotime. *Reviews in Mineralogy and Geochemistry*, *48*(1), 559–577. https://doi.org/10.2138/rmg.2002.48.15

Farley, K. A., Wolf, R. A., & Silver, L. T. (1996). The effects of long alpha-stopping distances on (U-Th)/He ages. *Geochimica et Cosmochimica Acta*, *60*(21), 4223–4229. https://doi.org/10.1016/s0016-7037(96)00193-7

Fayon, A. K., Peacock, S. M., Stump, E., & Reynolds, S. J. (2000). Fission track analysis of the footwall of the Catalina detachment fault, Arizona: Tectonic denudation, magmatism, and erosion. *Journal of Geophysical Research*, *105*(B5), 11047–11062. https://doi.org/10.1029/1999jb900421

Fitzgerald, P. G., Reynolds, S. J., Stump, E., Foster, D. A., & Gleadow, A. J. W. (1993). Thermochronologic evidence for timing of denudation and rate of crustal extension of the South Mountains metamorphic core complex and Sierra Estrella, Arizona. *Nuclear Tracks and Radiation Measurements*, *21*(4), 555–563. https://doi.org/10.1016/1359-0189(93)90196-g

Flowers, R. M., Ketcham, R. A., Enkelmann, E., Gautheron, C., Reiners, P. W., Metcalf, J. R., et al. (2023). (U-Th)/He chronology: Part 2. Considerations for evaluating, integrating, and interpreting conventional individual aliquot data. *Geological Society of America Bulletin*, *135*(1–2), 137–161. https://doi.org/10.1130/b36268.1

Flowers, R. M., Ketcham, R. A., Shuster, D. L., & Farley, K. A. (2009). Apatite (U–Th)/He thermochronometry using a radiation damage accumulation and annealing model. *Geochimica et Cosmochimica Acta*, *73*(8), 2347–2365. https://doi.org/10.1016/j.gca.2009.01.015

Flowers, R. M., Zeitler, P. K., Danišík, M., Reiners, P. W., Gautheron, C., Ketcham, R. A., et al. (2023). (U-Th)/He chronology: Part 1. Data, uncertainty, and reporting. *Geological Society of America Bulletin*, *135*(1–2), 104–136. https://doi.org/10.1130/b36266.1

Foster, D. A., Gleadow, A. J., Reynolds, S. J., & Fitzgerald, P. G. (1993). Denudation of metamorphic core complexes and the reconstruction of the transition zone, west central Arizona: Constraints from apatite fission track thermochronology. *Journal of Geophysical Research*, *98*(B2), 2167–2185. https://doi.org/10.1029/92jb02407

Foster, D. A., & John, B. E. (1999). Quantifying tectonic exhumation in an extensional orogen with thermochronology: Examples from the southern Basin and Range province. *Geological Society of London Special Publication*, *154*(1), 343–364. https://doi.org/10.1144/gsl.sp.1999.154.01.16

Foster, D. A., & Spencer, J. E. (1992). Apatite and zircon fission-track dates from the northern Plomosa Mountains, La Paz County, west-central Arizona. Arizona Geological Survey Open File Report 92-09.

Furlong, K. P., & Schwartz, S. Y. (2004). Influence of the Mendocino triple junction on the tectonics of coastal California. *Annual Review of Earth and Planetary Sciences*, *32*(1), 403–433. https://doi.org/10.1146/annurev.earth.32.101802.120252

Galbraith, R. F. (2005). *Statistics for fission track analysis* (Vol. 165, p. 219). Chapman and Hall/CRC.

Gans, P. B., Mahood, G. A., & Schermer, E. (1989). Synextensional magmatism in the Basin and Range province: A case study from the eastern great basin. Geological Society of America Special Paper (Vol. *233*, p. 53).

Gautheron, C., Djimbi, D. M., Roques, J., Balout, H., Ketcham, R. A., Simoni, E., et al. (2020). A multi-method, multi-scale theoretical study of He and Ne diffusion in zircon. *Geochimica et Cosmochimica Acta*, *268*, 348–367. https://doi.org/10.1016/j.gca.2019.10.007

Ginster, U., Reiners, P. W., Nasdala, L., & Chanmuang, C. (2019). Annealing kinetics of radiation damage in zircon. *Geochimica et Cosmochimica Acta*, *249*, 225–246. https://doi.org/10.1016/j.gca.2019.01.033

Glazner, A. F., & Bartley, J. M. (1984). Timing and tectonic setting of Tertiary low-angle normal faulting and associated magmatism in the southwestern United States. *Tectonics*, *3*, 385–396. https://doi.org/10.1029/tc003i003p00385

Gleadow, A. J. W., & Lovering, J. F. (1977). Geometry factor for external detectors in fission track dating. *Nuclear Track Detection*, *1*(2), 99–106. https://doi.org/10.1016/0145-224x(77)90003-5

Gottardi, R., McAleer, R., Casale, G., Borel, M., Iriondo, A., & Jepson, G. (2020). Exhumation of the Coyote Mountains metamorphic core complex (Arizona): Implications for orogenic collapse of the southern North American Cordillera. *Tectonics*, *39*(8), e2019TC006050. https://doi.org/10.1029/2019tc006050

Granillo, R. V., & Calmus, T. (2003). Mazatán metamorphic core complex (Sonora, Mexico): Structures along the detachment fault and its exhumation evolution. *Journal of South American Earth Sciences*, *16*(4), 193–204. https://doi.org/10.1016/s0895-9811(03)00066-x

Guenthner, W. R. (2021). Implementation of an alpha damage annealing model for zircon (U-Th)/He thermochronology with comparison to a zircon fission track annealing model. *Geochemistry, Geophysics, Geosystems*, *22*(2), e2019GC008757. https://doi.org/10.1029/2019gc008757

Guenthner, W. R., Reiners, P. W., Ketcham, R. A., Nasdala, L., & Giester, G. (2013). Helium diffusion in natural zircon: Radiation damage, anisotropy, and the interpretation of zircon (U-Th)/He thermochronology. *American Journal of Science*, *313*(3), 145–198. https://doi.org/10.2475/03.2013.01

Haines, S. H., & van der Pluijm, B. A. (2008). Clay quantification and Ar–Ar dating of synthetic and natural gouge: Application to the Miocene Sierra Mazatán detachment fault, Sonora, Mexico. *Journal of Structural Geology*, *30*(4), 525–538. https://doi.org/10.1016/j.jsg.2007.11.012

Henry, C. D., Price, J. G., & James, E. W. (1991). Mid-Cenozoic stress evolution and magmatism in the Southern Cordillera, Texas and Mexico: Transition from continental arc to intraplate extension. *Journal of Geophysical Research*, *96*(B8), 13545–13560. https://doi.org/10.1029/91jb00202

Hourigan, J. K., Reiners, P. W., & Brandon, M. T. (2005). U-Th zonation-dependent alpha-ejection in (U-Th)/He chronometry. *Geochimica et Cosmochimica Acta*, *69*(13), 3349–3365. https://doi.org/10.1016/j.gca.2005.01.024

Howlett, C. J., Reynolds, A. N., & Laskowski, A. K. (2021). Magmatism and extension in the Anaconda metamorphic core complex of western Montana and relation to regional tectonics. *Tectonics*, *40*(9), e2020TC006431. https://doi.org/10.1029/2020tc006431

Hurford, A. J., & Green, P. F. (1983). The zeta age calibration of fission-track dating. *Chemical Geology*, *41*, 285–317. https://doi.org/10.1016/s0009-2541(83)80026-6

Jacobson, C. E., Jacques-Ayala, C., Barth, A. P., García y Barragán, J. C., Pedrick, J. N., & Wooden, J. L. (2019). Protolith age of the Altar and Carnero complexes and latest Cretaceous–Miocene deformation in the Caborca–Altar region of northwestern Sonora, Mexico. *Revista Mexicana de Ciencias Geológicas*, *36*(1), 95–109. https://doi.org/10.22201/cgeo.20072902e.2019.1.784

Jepson, G., Carrapa, B., George, S. W., Reeher, L. J., Kapp, P. A., Davis, G. H., et al. (2022). Where did the Arizona-Plano go? Protracted thinning via upper-to lower-crustal processes. *Journal of Geophysical Research: Solid Earth*, *127*(4), e2021JB023850. https://doi.org/10.1029/2021jb023850

Jepson, G., Carrapa, B., George, S. W., Triantafyllou, A., Egan, S. M., Constenius, K. N., et al. (2021). Resolving mid-to upper-crustal exhumation through apatite petrochronology and thermochronology. *Chemical Geology*, *565*, 120071. https://doi.org/10.1016/j.chemgeo.2021.120071

John, B. E., & Foster, D. A. (1993). Structural and thermal constraints on the initiation angle of detachment faulting in the southern Basin and Range: The Chemehuevi Mountains case study. *Geological Society of America Bulletin*, *105*(8), 1091–1108. https://doi.org/10.1130/0016-7606(1993)105<1091:satcot>2.3.co;2

Ketcham, R. A. (2005). Forward and inverse modeling of low-temperature thermochronometry data. *Reviews in Mineralogy and Geochemistry*, *58*(1), 275–314. https://doi.org/10.2138/rmg.2005.58.11

Konstantinou, A. (2022). The "death" of the Sevier-Laramide orogen: Gravitational collapse of the crust or something else? In J. P. Craddock, D. H. Malone, B. Z. Foreman, & A. Konstantinou (Eds.) *Tectonic evolution of the Sevier-Laramide Hinterland, thrust belt, and foreland, and postorogenic slab rollback (180–20 Ma)*. Geological Society of America Special Paper (Vol. 555).

Konstantinou, A., & Miller, E. (2015). Evidence for a long-lived accommodation/transfer zone beneath the Snake River Plain: A possible influence on Neogene magmatism? *Tectonics*, *34*(12), 2387–2398. https://doi.org/10.1002/2015tc003863

Kruger, J. M., & Johnson, R. A. (1994). Raft model of crustal extension: Evidence from seismic reflection data in southeast Arizona. *Geology*, *22*(4), 351–354. https://doi.org/10.1130/0091-7613(1994)022<0351:rmocee>2.3.co;2

Kruger, J. M., Johnson, R. A., & Houser, B. B. (1995). Miocene-Pliocene half-graben evolution, detachment faulting and late-stage core complex uplift from reflection seismic data in south-east Arizona. *Basin Research*, *7*(2), 129–149. https://doi.org/10.1111/j.1365-2117.1995.tb00100.x

Kuiper, K. F., Deino, A., Hilgen, F. J., Krijgsman, W., Renne, P. R., & Wijbrans, A. J. (2008). Synchronizing rock clocks of Earth history. *Science*, *320*(5875), 500–504. https://doi.org/10.1126/science.1154339

LaForge, J. S., John, B. E., & Grimes, C. B. (2017). Synextensional dike emplacement across the footwall of a continental core complex, Chemehuevi Mountains, southeastern California. *Geosphere*, *13*(6), 1867–1886. https://doi.org/10.1130/ges01402.1

Lee, J. Y., Marti, K., Severinghaus, J. P., Kawamura, K., Yoo, H. S., Lee, J. B., & Kim, J. S. (2006). A redetermination of the isotopic abundances of atmospheric Ar. *Geochimica et Cosmochimica Acta*, *70*(17), 4507–4512. https://doi.org/10.1016/j.gca.2006.06.1563

Long, K. B., Gehrels, G. E., & Baldwin, S. L. (1995). Tectonothermal evolution of the Pinaleño-Jackson Mountain core complex, southeast Arizona. *Geological Society of America Bulletin*, *107*(10), 1231–1240. https://doi.org/10.1130/0016-7606(1995)107<1231:teotpo>2.3.co;2

Lund-Snee, J. E., & Miller, E. L. (2022). Magmatism, migrating topography, and the transition from Sevier shortening to Basin and Range extension, western United States. In J. P. Craddock, D. H. Malone, B. Z. Foreman, & A. Konstantinou (Eds.) (Vol. 555). Geological Society of America Special Paper. *Tectonic evolution of the sevier-Laramide Hinterland, thrust belt, and foreland, and postorogenic slab rollback (180–20 Ma)*.

Meijer, A. (2014). The Pinal Schist of southern Arizona: A paleoproterozoic forearc complex with evidence of spreading ridge–trench interaction at ca. 1.65 Ga and a Proterozoic arc obduction event. *Geological Society of America Bulletin*, *126*(9–10), 1145–1163. https://doi.org/10.1130/b31002.1

Min, K., Mundil, R., Renne, P. R., & Ludwig, K. R. (2000). A test for systematic errors in $^{40}Ar/^{39}Ar$ geochronology through comparison with U/Pb analysis of a 1.1-Ga rhyolite. *Geochimica et Cosmochimica Acta*, *64*(1), 73–98. https://doi.org/10.1016/s0016-7037(99)00204-5

Miranda-Gasca, M. A., Gomez-Caballero, J. A., & Eastoe, C. J. (1998). Borate deposits of northern Sonora, Mexico; stratigraphy, tectonics, stable isotopes, and fluid inclusions. *Economic Geology*, *93*(4), 510–523. https://doi.org/10.2113/gsecongeo.93.4.510

Müller, R. D., Cannon, J., Qin, X., Watson, R. J., Gurnis, M., Williams, S., et al. (2018). GPlates: Building a virtual Earth through deep time. *Geochemistry, Geophysics, Geosystems*, *19*(7), 2243–2261. https://doi.org/10.1029/2018gc007584

Müller, R. D., Zahirovic, S., Williams, S. E., Cannon, J., Seton, M., Bower, D. J., et al. (2019). A global plate model including lithospheric deformation along major rifts and orogens since the Triassic. *Tectonics*, *38*(6), 1884–1907. https://doi.org/10.1029/2018tc005462

Murray, K. E., Goddard, A. L. S., Abbey, A. L., & Wildman, M. (2022). Thermal history modeling techniques and interpretation strategies: Applications using HeFTy. *Geosphere*, *18*(5), 1622–1642. https://doi.org/10.1130/ges02500.1

Naruk, S. J. (1986). Strain and displacement across the Pinaleño Mountains shear zone, Arizona, USA. *Journal of Structural Geology*, *8*(1), 35–46. https://doi.org/10.1016/0191-8141(86)90015-5

Nickerson, P. A. (2012). *Post-mineral normal faulting in Arizona porphyry systems* (Ph.D. dissertation). University of Arizona.

Nourse, J. A., Anderson, T. H., & Silver, L. T. (1994). Tertiary metamorphic core complexes in Sonora, northwestern Mexico. *Tectonics*, *13*(5), 1161–1182. https://doi.org/10.1029/93tc03324

Pease, V., Foster, D., Wooden, J., O'Sullivan, P., Argent, J., & Fanning, C. (1999). The Northern Sacramento Mountains, southwest United States. Part II: Exhumation history and detachment faulting. Geological Society, London, Special Publication (Vol. *164*, pp. 199–238).

Platt, J. P., Behr, W. M., & Cooper, F. J. (2015). Metamorphic core complexes: Windows into the mechanics and rheology of the crust. *Journal of the Geological Society*, *172*(1), 9–27. https://doi.org/10.1144/jgs2014-036

Price, J. G., & Henry, C. D. (1984). Stress orientations during Oligocene volcanism in Trans-Pecos Texas: Timing the transition from Laramide compression to Basin and range tension. *Geology*, *12*(4), 238–241. https://doi.org/10.1130/0091-7613(1984)12<238:sodovi>2.0.co;2

Prior, M. G., Stockli, D. F., & Singleton, J. S. (2016). Miocene slip history of the Eagle Eye detachment fault, Harquahala Mountains metamorphic core complex, west-central Arizona. *Tectonics*, *35*(8), 1913–1934. https://doi.org/10.1002/2016tc004241

Reade, N. Z., Biddle, J. M., Ricketts, J. W., Amato, J. M., & Roeske, S. (2020). Zircon (U-Th)/He thermochronologic constraints on the long-term thermal evolution of southern New Mexico and western Texas. *Lithosphere*, *1*, 8881315. https://doi.org/10.2113/2020/8881315

Rehrig, W. A., & Reynolds, S. (1980). Geologic and geochronologic reconnaissance of a northwest-trending zone of metamorphic core complexes in southern and western Arizona. In M. D. Crittenden, P. J. Coney, & G. H. Davis (Eds.) (Vol. 153, pp. 131–157). *Cordilleran metamorphic core complexes*, Geological Society of America Memoir.

Reiners, P. W. (2005). Zircon (U-Th)/He thermochronometry. *Reviews in Mineralogy and Geochemistry*, *58*(1), 151–179. https://doi.org/10.2138/rmg.2005.58.6

Reiners, P. W., & Brandon, M. T. (2006). Using thermochronology to understand orogenic erosion. *Annual Review of Earth and Planetary Sciences*, *34*(1), 419–466. https://doi.org/10.1146/annurev.earth.34.031405.125202

Reiners, P. W., Spell, T. L., Nicolescu, S., & Zanetti, K. A. (2004). Zircon (U-Th)/He thermochronometry: He diffusion and comparisons with $^{40}Ar/^{39}Ar$ dating. *Geochimica et Cosmochimica Acta*, *68*(8), 1857–1887. https://doi.org/10.1016/j.gca.2003.10.021

Rey, P. F., Teyssier, C., & Whitney, D. L. (2009). Extension rates, crustal melting, and core complex dynamics. *Geology*, *37*(5), 391–394. https://doi.org/10.1130/g25460a.1

Ross, J. (2019). NMGRL/pychron (version 18.2) [Software]. *Zenodo*. https://doi.org/10.5281/zenodo.3237834

Schaen, A. J., Jicha, B. R., Hodges, K. V., Vermeesch, P., Stelten, M. E., Mercer, C. M., et al. (2021). Interpreting and reporting $^{40}Ar/^{39}Ar$ geochronologic data. *Geological Society of America Bulletin*, *133*(3–4), 461–487. https://doi.org/10.1130/b35560.1

Scoggin, S. H., Chapman, J. B., Shields, J. E., Trzinski, A. E., & Ducea, M. N. (2021). Early Paleogene Magmatism in the Pinaleño Mountains, Arizona: Evidence for crustal melting of diverse basement assemblages during the Laramide orogeny. *Journal of Petrology*, *62*(12), egab095. https://doi.org/10.1093/petrology/egab095

Scoggin, S. H., Reiners, P. W., Shuster, D. L., Davis, G. H., Ward, L. A., Worthington, J. R., et al. (2021). (U-Th)/He and $^{4}He/^{3}He$ thermochronology of secondary oxides in faults and fractures: A regional perspective from southeastern Arizona. *Geochemistry, Geophysics, Geosystems*, *22*(12), e2021GC009905. https://doi.org/10.1029/2021gc009905

Severinghaus, J., & Atwater, T. (1990). Cenozoic geometry and thermal state of the subducting slabs beneath western North America. In B. P. Wernicke (Ed.) (Vol. 176, pp. 1–22), *Basin and range extensional tectonics near the latitude of Las Vegas, Nevada*. Geological Society of America Memoir.

Singleton, J. S., Seymour, N. M., Reynolds, S. J., Vomocil, T., & Wong, M. S. (2019). Distributed Neogene faulting across the western to central Arizona metamorphic core complex belt: Synextensional constriction and superposition of the Pacific–North America plate boundary on the southern Basin and Range. *Geosphere*, *15*(4), 1409–1435. https://doi.org/10.1130/ges02036.1

Singleton, J. S., Stockli, D. F., Gans, P. B., & Prior, M. G. (2014). Timing, rate, and magnitude of slip on the Buckskin-Rawhide detachment fault, west central Arizona. *Tectonics*, *33*(8), 1596–1615. https://doi.org/10.1002/2013tc003517

Sonder, L. J., & Jones, C. H. (1999). Western United States extension: How the west was widened. *Annual Review of Earth and Planetary Sciences*, *27*(1), 417–462. https://doi.org/10.1146/annurev.earth.27.1.417

Spencer, J. E., Richard, S. M., & Ferguson, C. A. (2001). Cenozoic structure and evolution of the boundary between the Basin and range and transition zone provinces in Arizona. In M. C. Erskine, J. E. Faulds, J. M. Bartley, & P. D. Rowley (Eds.), *The geologic transition, high plateaus to great basin: A symposium and field guide: The Mackin Volume* (Vol. 30, pp. 273–289). Utah Geological Association Publication.

Spencer, J. E., Richard, S. M., Reynolds, S. J., Miller, R. J., Shafiqullah, M., Gilbert, W. G., & Grubensky, M. J. (1995). Spatial and temporal relationships between mid-Tertiary magmatism and extension in southwestern Arizona. *Journal of Geophysical Research*, *100*(B6), 10321–10351. https://doi.org/10.1029/94jb02817

Thorman, C. H., & Naruk, S. J. (1987). Generalized bedrock geologic map and distribution of mylonitic rocks in the eastern Pinaleño Mountains, Graham County, Arizona. U.S. Geological Survey Open File Report (Vol. *87*, p. 614).

Wagner, G., & Van den Haute, P. (2012). *Fission-track dating* (Vol. 6, pp. 1–285). Springer.

Whitney, D. L., Teyssier, C., Rey, P., & Buck, W. R. (2013). Continental and oceanic core complexes. *Geological Society of America Bulletin*, *125*(3–4), 273–298. https://doi.org/10.1130/b30754.1

Wong, M. S., & Gans, P. B. (2008). Geologic, structural, and thermochronologic constraints on the tectonic evolution of the Sierra Mazatán core complex, Sonora, Mexico: New insights into metamorphic core complex formation. *Tectonics*, *27*(4), TC4013. https://doi.org/10.1029/2007tc002173

Wong, M. S., Gans, P. B., & Scheier, J. (2010). The $^{40}Ar/^{39}Ar$ thermochronology of core complexes and other basement rocks in Sonora, Mexico: Implications for Cenozoic tectonic evolution of northwestern Mexico. *Journal of Geophysical Research*, *115*(B7), B07414. https://doi.org/10.1029/2009jb007032

Zuza, A. V., & Cao, W. (2023). Metamorphic core complex dichotomy in the North American Cordillera explained by buoyant upwelling in variably thick crust. *Geological Society of America Today*, *33*(3–4), 4–11. https://doi.org/10.1130/GSATG548A.1